
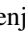












# Rocks with Extremely Low Thermal Inertia at the OSIRIS-REx Sample Site on Asteroid Benu

Andrew J. Ryan<sup>1,13</sup> , Benjamin Rozitis<sup>2</sup> , Daniel Pino Munoz<sup>3</sup>, Kris J. Becker<sup>1</sup>, Joshua P. Emery<sup>4</sup> , Michael C. Nolan<sup>1</sup>, Marc Bernacki<sup>3</sup>, Marco Delbo<sup>5</sup> , Catherine M. Elder<sup>6</sup> , Matthew Siegler<sup>7,8</sup>, Erica R. Jawin<sup>9</sup>, Dathon R. Golish<sup>1</sup> , Kevin J. Walsh<sup>10</sup> , Christopher W. Haberle<sup>4</sup>, Carina A. Bennett<sup>1</sup>, Kenneth L. Edmundson<sup>1</sup> , Victoria E. Hamilton<sup>10</sup>, Phillip R. Christensen<sup>11</sup>, Michael G. Daly<sup>12</sup> , and Dante S. Lauretta<sup>1</sup> 

<sup>1</sup>Lunar and Planetary Laboratory, University of Arizona, Tucson, AZ 85721, USA; [ajryan4@arizona.edu](mailto:ajryan4@arizona.edu)

<sup>2</sup>School of Physical Sciences, The Open University, Milton Keynes, MK7 6AA, UK

<sup>3</sup>Mines Paris, PSL University, Centre for material forming (CEMEF), UMR7635 CNRS, 06904 Sophia Antipolis, France

<sup>4</sup>Department of Astronomy and Planetary Science, Northern Arizona University, Flagstaff, AZ 86011-6010, USA

<sup>5</sup>Université Côte d'Azur, Observatoire de la Côte d'Azur, CNRS, Laboratoire Lagrange, CS 34229, F-06304 Nice Cedex 4, France

<sup>6</sup>Jet Propulsion Laboratory, California Institute of Technology, Pasadena, CA 91011, USA

<sup>7</sup>Planetary Science Institute, Tucson, AZ 85719-2395, USA

<sup>8</sup>Department of Earth Sciences, Southern Methodist University, Dallas, TX 75275, USA

<sup>9</sup>Smithsonian Institution National Air and Space Museum, Washington, DC 20560, USA

<sup>10</sup>Southwest Research Institute, Boulder, CO 80302, USA

<sup>11</sup>School of Earth and Space Exploration, Arizona State University, Tempe, AZ 85287-6004, USA

<sup>12</sup>The Centre for Research in Earth and Space Science, York University, Toronto, ON, M3J 1P3, Canada

Received 2023 November 17; revised 2024 January 23; accepted 2024 February 14; published 2024 April 4

## Abstract

The Origins, Spectral Interpretation, Resource Identification, and Security–Regolith Explorer (OSIRIS-REx) mission recently returned a sample of rocks and dust collected from asteroid Benu. We analyzed the highest-resolution thermal data obtained by the OSIRIS-REx Thermal Emission Spectrometer (OTES) to gain insight into the thermal and physical properties of the sampling site, including rocks that may have been sampled, and the immediately surrounding Hokioi Crater. After correcting the pointing of the OTES data sets, we find that OTES fortuitously observed two dark rocks moments before they were contacted by the spacecraft. We derived thermal inertias of 100–150 ( $\pm 50$ ) J m<sup>-2</sup> K<sup>-1</sup> s<sup>-1/2</sup> for these two rocks—exceptionally low even compared with other previously analyzed dark rocks on Benu (180–250 J m<sup>-2</sup> K<sup>-1</sup> s<sup>-1/2</sup>). Our simulations indicate that monolayer coatings of sand- to pebble-sized particles, as observed on one of these rocks, could significantly reduce the apparent thermal inertia and largely mask the properties of the substrate. However, the other low-thermal-inertia rock that was contacted is not obviously covered in particles. Moreover, this rock appears to have been partially crushed, and thus potentially sampled, by the spacecraft. We conclude that this rock may be highly fractured and that it should be sought in the returned sample to better understand its origin in Benu's parent body and the relationship between its thermal and physical properties.

*Unified Astronomy Thesaurus concepts:* Asteroids (72); Asteroid surfaces (2209); Planetary science (1255); Remote sensing (2191); Near-Earth objects (1092)

## 1. Introduction

NASA's Origins, Spectral Interpretation, Resource Identification, and Security–Regolith Explorer (OSIRIS-REx) mission collected pristine samples of regolith from asteroid (101955) Benu on 2020 October 20, in a brief touchdown sequence known as the Touch-and-Go (TAG) maneuver (Lauretta et al. 2022). The spacecraft contacted Benu's surface with its Touch-and-Go Sample Acquisition Mechanism (TAGSAM; Bierhaus et al. 2018), fired a burst of nitrogen gas to drive regolith into the collection chamber, and backed away seconds later. The samples were returned to Earth on 2023 September 24, for detailed mineralogical, organic, isotopic, spectral, and thermophysical analysis (Lauretta et al. 2023a).

Benu was studied extensively by the OSIRIS-REx instrument suite prior to the TAG maneuver (see Lauretta et al. 2019, 2021, and references therein). The rugged surface of the asteroid is covered almost ubiquitously with meter-scale and larger boulders, with very few regions exhibiting fine-grained regolith suitable for sampling (e.g., Walsh et al. 2019). Two globally abundant boulder types—one very dark and one modestly brighter—were identified on the basis of visible-wavelength reflectance and color data, which could indicate heterogeneity in Benu's parent body (DellaGiustina et al. 2019, 2020).

Global thermophysical analysis corroborated the presence of two dominant lithologies by finding that the lower-reflectance boulders have distinctly lower thermal inertia, indicative of lower thermal conductivity, density, and strength, compared to their higher-reflectance counterparts (Rozitis et al. 2020b; Cambioni et al. 2021). These properties furthermore appear to be largely distinct from those of carbonaceous meteorites (e.g., Flynn et al. 2018; Opeil et al. 2020). Namely, both of Benu's dominant boulder types are inferred to have higher porosity (lower density), lower thermal conductivity, and potentially lower strength than meteorites with spectroscopic features

<sup>13</sup> Corresponding author.



Original content from this work may be used under the terms of the [Creative Commons Attribution 4.0 licence](https://creativecommons.org/licenses/by/4.0/). Any further distribution of this work must maintain attribution to the author(s) and the title of the work, journal citation and DOI.

similar to those of Bennu (Hamilton et al. 2019). A more recent study of Bennu’s boulders indicated that the two dominant types may consist of multiple distinct subtypes on the basis of morphology and roughness (Jawin et al. 2023); the dark boulders are subdivided into boulder Types A and B, while the bright boulders are subdivided into Types C and D, largely on the basis of morphology. It is not yet known if these subtypes are also distinct in thermal and physical properties.

After a thorough campaign to identify a feasible sampling location on Bennu, four finalist sites were identified, all in impact craters. These sites were investigated at increasing spatial resolution in a series of reconnaissance flybys (Recons A, B, and C; Lauretta et al. 2021; Rozitis et al. 2022). Ultimately, the site dubbed Nightingale (approximate center coordinates  $56^\circ$ ,  $43^\circ$ ) in Hokioi Crater was chosen for its abundant sampleable regolith particles—centimeter-scale and smaller—and relatively few hazards to the spacecraft. Nightingale was found to have a low thermal inertia of  $190 \pm 30 \text{ J m}^{-2} \text{ K}^{-1} \text{ s}^{-1/2}$ , compared to the global average of  $\sim 300 \text{ J m}^{-2} \text{ K}^{-1} \text{ s}^{-1/2}$ , likely due to the abundant particulate regolith (Rozitis et al. 2022). This value is consistent with a median regolith particle size of  $\sim 0.5\text{--}2.0$  cm, which is within the range of particle sizes observed in high-resolution images of Nightingale (Burke et al. 2021) and in photos of particles drifting out of the TAGSAM following sample collection (Lauretta et al. 2022). The rocks and fine particles in Hokioi Crater and at the TAG contact location are predominantly of the darker lithology, excavated from  $<1.5$  m depth during the formation of the crater, and secondarily of the brighter lithology, likely derived from regolith surrounding the crater (Barnouin et al. 2022; Lauretta et al. 2022; Jawin et al. 2023). Further interpretation of the physical properties of individual boulders and fine regolith has been somewhat limited by the spot size of observations obtained by the OSIRIS-REx Thermal Emission Spectrometer (OTES; Christensen et al. 2018).

The TAG sampling event mobilized rocks and dust into a debris plume, significantly disrupting the Nightingale site by forming a 9 m long elliptical crater within Hokioi Crater (Lauretta et al. 2022). High-resolution images obtained by the SamCam imager ( $\sim 1$  mm pixel $^{-1}$ ) in the OSIRIS-REx Camera Suite (OCAMS; Rizk et al. 2018; Golish et al. 2020) immediately preceding and during the initial moments of sample collection revealed that the TAGSAM contacted and may have partially disrupted or crushed a  $\sim 20$  cm long dark rock, referred to herein as the “tagged rock,” located on the western edge of the contact point (Lauretta et al. 2022; Walsh et al. 2022). A  $\sim 40$  cm long boulder, referred to herein as the “plate rock,” just to the southwest of the TAG point appeared to act as a rigid plate—it was levered upward by the TAGSAM contact and launched millimeter- to centimeter-scale particles that had been perched on its surface (Lauretta et al. 2022; Walsh et al. 2022).

The forces measured by the spacecraft during the initial  $\sim 1$  s that TAGSAM penetrated the surface (before the nitrogen gas for sampling was fired) were consistent with a granular bed with near-zero cohesion and a bulk density  $440\text{--}600 \text{ kg m}^{-3}$  (Walsh et al. 2022)—less than half that of the bulk asteroid ( $\sim 1190 \text{ kg m}^{-3}$ ; Scheeres et al. 2019). Analysis of the post-TAG crater corroborated these findings (Lauretta et al. 2022). The difference in density was attributed to a lower regolith packing fraction ( $\leq \sim 0.5$ ) compared to the bulk asteroid

( $\sim 0.85\text{--}0.88$ ) (Biele et al. 2020; Tricarico et al. 2021; Walsh et al. 2022).

In this work, we analyzed the highest-resolution OTES data available of Hokioi Crater to gain insight into the thermal and physical properties of the TAG site and its immediate surroundings. Given the observation of particles coating the plate rock, we also performed 3D thermal modeling to understand how such coatings could affect the apparent thermal inertia of the rocks. This work represents a final effort to obtain a remote-sensing perspective of asteroid Bennu and the properties and context of the OSIRIS-REx sample before we ground truth our findings via laboratory analyses. In addition to verifying the existence of two lithologies with distinct thermophysical properties, sample analysis will also give insight into the physical properties of Bennu as a potentially hazardous near-Earth impactor (Lauretta et al. 2023a).

## 2. Methods

### 2.1. Checkpoint, Matchpoint, and TAG Data

The OSIRIS-REx spacecraft performed two rehearsals—Checkpoint and Matchpoint—followed by the TAG sample-collection maneuver. In all three passes, OTES was turned on as a “ride-along” instrument, collecting point spectra (“spots”) on the surface of wherever the spacecraft happened to be pointed. In all three data sets, summarized in Table 1, OTES pointed outside of Hokioi Crater (approximately southeast) before eventually pointing within it. As shown later, the OTES instrument fortuitously observed portions of the TAG site.

All OTES spot diameters during these observations were approximately 1 m or smaller—considerably higher spatial resolution than OTES data sets from previous mission phases, including the global survey ( $\sim 40$  m; Rozitis et al. 2020b; Cambioni et al. 2021), Recon A ( $\sim 8$  m; Rozitis et al. 2020b, 2022); Recon B ( $\sim 5$  m) and Recon C ( $\sim 2.5$  m; Rozitis et al. 2022), which have been analyzed in other studies.

### 2.2. Thermophysical Model for OTES Matchpoint, Checkpoint, and TAG Data

We use the variant of the Advanced Thermophysical Model (ATPM; Rozitis & Green 2011) that has previously been adapted for use on Bennu (DellaGiustina et al. 2019; Rozitis et al. 2020a, 2020b, 2022) to model the surface temperature of Hokioi Crater. The model solves the 1D heat equation for each triangular facet of a 20 cm spatial resolution digital terrain model (DTM), described below, assuming unchanging material properties with depth. The surface boundary condition includes solar heating (accounting for shadows cast by nearby topographic features), radiative heat loss to space, and surface-to-surface heating (i.e., “self-heating”) via radiative heat transfer between nearby facets that share direct line of sight. This model does not account for lateral conduction of heat, which should be minimal even at these length scales due to the low thermal conductivity of the surface materials on Bennu. The ATPM ultimately generates a look-up table of brightness temperature and radiance spectra as a function of surface thermal inertia for each OTES spot location and observation time. This table is compared to OTES radiance spectra to determine the best-fit thermal inertia values.

We applied the ATPM exactly as described by Rozitis et al. (2022). We used the v20 and v21 Poisson-reconstructed DTMs of Hokioi Crater and the immediately surrounding terrain

**Table 1**  
Summary of Data Sets Used in This Study

Observing Pass	Date and Time Span (UTC)	Spacecraft Minimum Range to Surface (m)	Number of OTES Observations Used	OTES Spot Diameters (Start, Minimum, End) (m)	Local Solar Hour (hr)	Phase Angle	Heliocentric Distance (au)	Heliocentric Longitude	Heliocentric Latitude
Checkpoint rehearsal	2020 April 14 22:37:11–22:49:10	65	288	1.04, 0.55, 0.67	13.2–14.2	63.0°– 65.4°	0.9171	98.18°	6.00°
Matchpoint rehearsal	2020 August 11 22:12:56–22:30:30	40	303	1.04, 0.33, 0.48	13.2–14.7	63.5°– 65.4°	1.2641	204.15°	–2.28°
TAG	2020 October 20 21:27:02–21:49:50	~0	550	1.04, 0.15, 0.15	13.2–15.1	64.6°– 65.4°	1.3547	245.17°	–5.39°

**Notes.** All OTES data are available on the Planetary Data System (PDS; Christensen et al. 2019). OTES spot diameters are calculated using the 8 mrad instrument field of view (Christensen et al. 2018). The minimum spot diameter is set by the diameter of the OTES primary mirror. We excluded OTES data with the phase-inversion issue that occurs when the instrument detector and target are at nearly the same temperature (Christensen et al. 2019) and TAG data collected after the TAGSAM gas was fired because of the disruption caused to the regolith surface.

(Daly et al. 2020; Seabrook et al. 2022), both of which were built using data obtained by the OSIRIS-REx Laser Altimeter (OLA; Daly et al. 2017). Other constant model parameters include a bolometric Bond albedo of 0.02 (Li et al. 2021), a bolometric emissivity of 0.95, a rotation period of 4.296 hr, and a pole orientation of  $\lambda_H = 69.92^\circ$  and  $\beta_H = -83.45^\circ$  (Lauretta et al. 2019). An empirical phase-angle correction was applied to the OTES radiance data before they were fit to the thermal model results to account for roughness effects that were not captured by the DTM itself. This correction was developed by Rozitis et al. (2022) when they found that thermal inertia solutions from the Recon A, B, and C mission phase OTES data for Hokiöi Crater (and the other candidate sample sites) varied systematically as a function of differences in observational phase angle and, to a lesser extent, local solar time between the three data sets. A set of wavelength-dependent coefficients was thus optimized to remove that residual trend. We apply the same correction to our results here (see Rozitis et al. 2022 for a detailed explanation).

The ATPM was initially run for all data sets (Table 1) using the OLA v20 DTM, as was used by Rozitis et al. (2022) for modeling of Recon observations. We then recomputed the TAG thermal model solutions using the revised OLA v21 DTM (Seabrook et al. 2022). The two DTMs are very similar. The primary difference is a small change of local elevation (v21 is 10 cm higher than v20) and a small lateral translation of the local terrain at the Nightingale site, neither of which would substantially affect the thermal result if the intersection of the OTES instrument boresight is properly determined for each model (discussed in Section 2.3). Despite the similarities between the DTMs, the TAG spot thermal inertia solutions change with a standard deviation of  $\pm 30 \text{ J m}^{-2} \text{ K}^{-1} \text{ s}^{-1/2}$  (Figures B1 and B2). The mean solution shifts by only  $1.3 \text{ J m}^{-2} \text{ K}^{-1} \text{ s}^{-1/2}$ . We attribute these differences to the extreme sensitivity of the daytime temperatures to subtle changes in topography at this scale, rather than as an indication that the v21 result is more accurate than the v20 result. The uncertainty in thermal inertia due to this terrain sensitivity is similar in magnitude to other sources of uncertainty, discussed below. We thus did not rerun the model for the Checkpoint and Matchpoint data using the v21 DTM given the considerable computational expense ( $\sim 1$  month wall-clock time) of each model run. When comparing thermal inertia results obtained from the two DTMs, we account for the lateral translation in the terrain.

There are four main sources of uncertainty in the determination of thermal inertia with the ATPM and OTES data:

1. *Noise in the OTES spectra.* Based on the instrumental brightness temperature uncertainty of 1 K (Christensen et al. 2018), we calculate the effects of spectral noise on thermal inertia by allowing a 1 K increase in allowable rms error (Equation 8 in Rozitis et al. 2022) for best-fit thermal inertia solutions. This results in a typical thermal inertia uncertainty of  $\pm 30 \text{ J m}^{-2} \text{ K}^{-1} \text{ s}^{-1/2}$ .
2. *Uncertainty from terrain sensitivity.* As described above, the comparisons between the v20 and v21 models give a standard deviation of  $30 \text{ J m}^{-2} \text{ K}^{-1} \text{ s}^{-1/2}$  in the thermal inertia derived for each OTES spot.
3. *Observation phase-angle correction.* We apply a wavelength-dependent brightness temperature correction based on phase angle. Checkpoint, Matchpoint, and TAG observations were all at a high phase angle of  $\sim 65^\circ$ . Based on uncertainty in the residual phase-angle linear

trend given by Rozitis et al. (2022), this gives a model residual uncertainty of  $\pm 1\text{--}2$  K, which introduces a thermal inertia uncertainty of  $20\text{--}30 \text{ J m}^{-2} \text{ K}^{-1} \text{ s}^{-1/2}$ .

4. *Uncertainty from spot offsets.* We used a Monte Carlo bootstrap method to estimate the effects of spot location uncertainty, following the global spot position adjustment described in Section 2.3. We performed 10,000 trials with different randomly chosen selections of OTES spots from each of the three phases, resulting in spot offset uncertainties of  $\sim 2$ ,  $\sim 4$ , and  $\sim 1$  cm for Checkpoint, Matchpoint, and TAG, respectively. If the spot offset uncertainty for Matchpoint (the largest uncertainty of the three) is propagated to thermal inertia, it results in a thermal inertia uncertainty of  $\sim 10 \text{ J m}^{-2} \text{ K}^{-1} \text{ s}^{-1/2}$ .

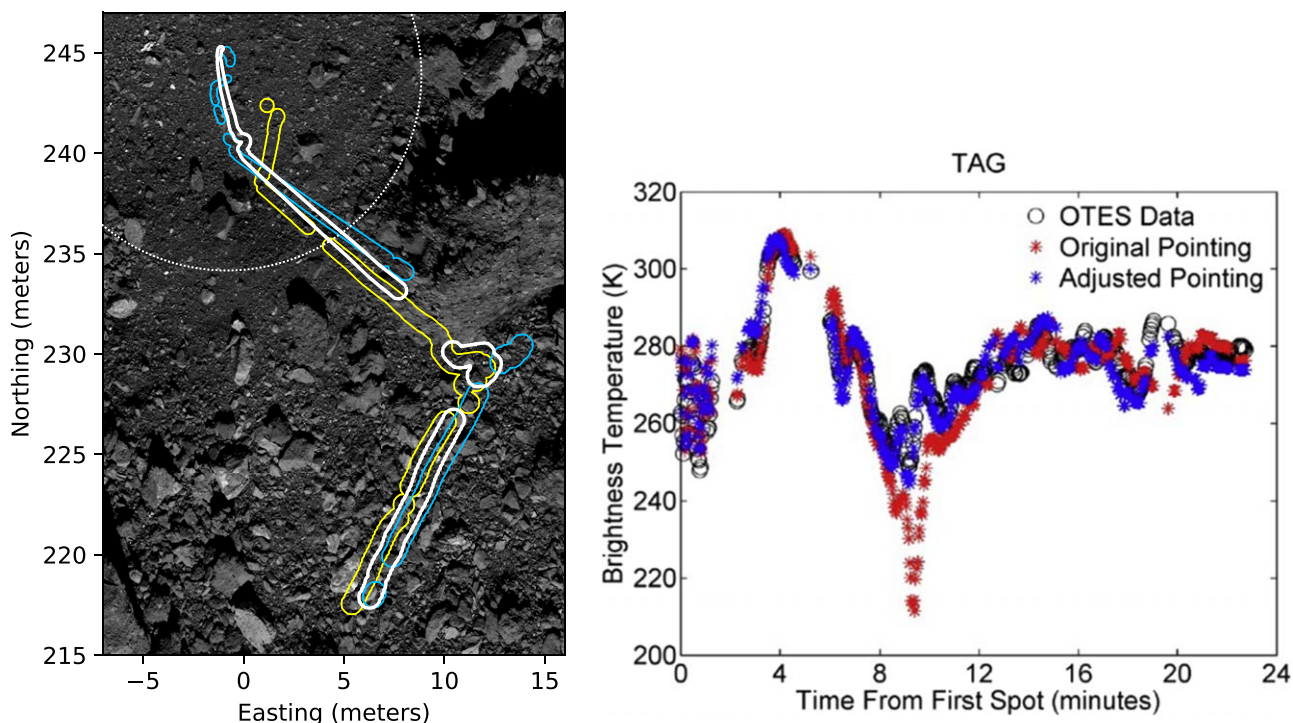
We can combine these four sources of uncertainty in quadrature,  $\sqrt{30^2 + 30^2 + 30^2 + 10^2}$ , which gives a total thermal inertia uncertainty of approximately  $\pm 50 \text{ J m}^{-2} \text{ K}^{-1} \text{ s}^{-1/2}$ . This uncertainty value is notably higher than in previous works, due mainly to the daytime-only nature of the observations, the very small spot sizes, and the pointing uncertainties. This larger uncertainty makes the quantitative interpretation of thermal inertia values more challenging, though we are still able to examine trends in relative thermal inertia with a high degree of confidence.

### 2.3. OTES Spot Location Determination

The precise position of the OTES boresight intersection on the surface of the asteroid (and thus the location of each observation) is calculated from spacecraft ephemeris and pointing kernels determined by the OSIRIS-REx team. Although these are generally of high quality, there is always some element of uncertainty in our absolute knowledge of spacecraft position and pointing with respect to the asteroid. Because OTES is a point spectrometer rather than an imager, pointing errors can be difficult to detect. Pointing uncertainties have not been discussed in previous studies because the uncertainties are far less consequential when the spot sizes are considerably larger (tens of meters). However, when analyzing the TAG and TAG rehearsal data, where the spots are much smaller—comparable in size to the spacecraft and the relative position offsets between individual instruments—pointing errors are more influential.

Issues with OTES spot location uncertainty were first identified when we conducted initial comparisons between TAG approach brightness temperatures measured by OTES and ATPM-predicted temperatures. There was a poor correspondence between the data and model predictions. We found that correspondence could be significantly improved by simply shifting all OTES spot locations northeast within a local reference frame around the crater (Figure 1, right), approximately 50 cm of offset in total (Figure B3). This shift also greatly improved the rms values for when individual OTES spot radiance spectra were fit to the model radiance spectra to determine best-fit thermal inertia values. The reduced error gave confidence that this was a valid approach to correcting for instrument pointing uncertainty. To ensure the validity of applying the same uniform offset to all spots (as opposed to a more complex pointing transformation), we calculated the optimal offset for the first half of the data set—outside of the crater and along the rim—to the optimal offset for the spots only within the central portion of the crater. The results were





**Figure 1.** Left: outlines of the extent of OTES observations collected during the Checkpoint (yellow), Matchpoint (blue), and TAG (white) observations, overlaid on a Recon A PolyCam mosaic. Gaps along the tracks are due to omitted data that had instrumental phase-inversion issues (Christensen et al. 2019). The dashed white circle marks the approximate rim of Hokioi Crater. The TAGSAM contact point is located approximately where the TAG and Matchpoint observations intersect and form a cross near the top of the image. Northing is given relative to the equator. Easting is given relative to the approximate center of Hokioi Crater. The specific northing/easting center was inconsequential to the analysis. Right: comparison between OTES  $9.24\ \mu\text{m}$  brightness temperatures and model-predicted brightness temperatures (using a mean global thermal inertia value and OLA v20 DTM) before and after the ATPM-based pointing adjustment.

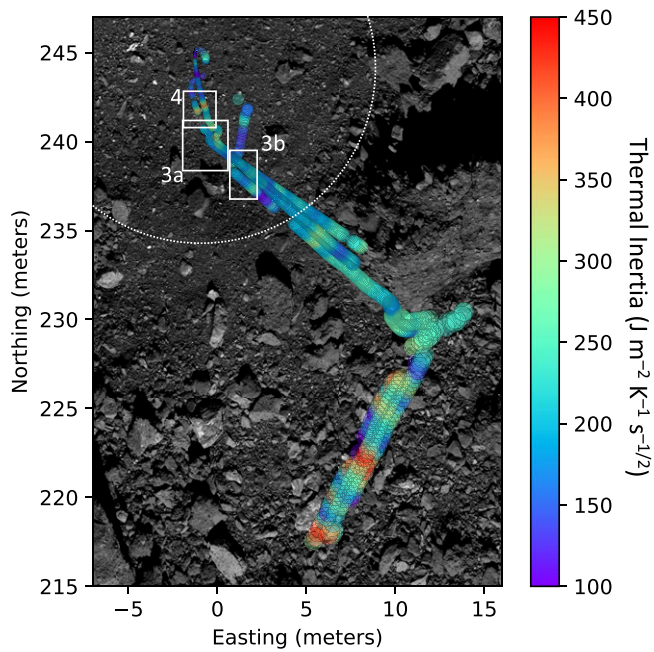
within 3.5 cm of each other (Figure B4). The same spot-location-correction approach was finally applied to calculating the pointing offset for the Checkpoint and Matchpoint data sets, resulting in spot shifts of 5 cm and 21 cm, respectively (Figure B3). We refer to this fitting of shifted data to the thermal model to minimize residuals as “ATPM-based” hereafter.

To independently verify the ATPM-based offsets, Becker & Edmundson (2024) correlated the OTES spot centers with spatially and temporally adjacent OCAMS images obtained near the end of the TAG approach, when the spacecraft trajectory was uniform, the image cadence was high, and the OTES spot size was small. The instruments are all fixed to the same observing platform, so their relative positions and orientations are constant. The OCAMS images obtained during the TAG descent (alternating between MapCam and SamCam) were controlled to an OLA v21 5 cm DTM within the crater and 40 cm DTM outside of the crater. This was accomplished by ground-truth control point mapping to the DTM and image-to-image feature matching of common ground coverage in OCAMS images, followed by a bundle adjustment to improve knowledge of the position and orientation of the camera with respect to the DTM (Bennett et al. 2021; Edmundson et al. 2020). Finally, with this improved pointing knowledge, the OTES spot locations were projected onto OCAMS images that overlapped and were closest in observation times to the OTES field of view (FOV). We were thereby able to visually verify the location of the OTES footprint with respect to the Bennu terrain as observed by OCAMS with an expected accuracy of  $\sim 10$  cm. The process is described in full detail in Becker & Edmundson (2024).

The mean spot offset from the image control was approximately 48 cm (Becker & Edmundson 2024), in good agreement with the 50 cm found from the ATPM-based approach. Importantly, we confirmed that the OTES spot locations near the TAG site determined with both approaches were in very good agreement—within 5 cm. However, earlier in the trajectory the spot locations from the two methods diverge in some places by tens of centimeters. We attribute this divergence to the lower image cadence as the spacecraft was maneuvering into position, leading to intervals where image-based pointing was not available for OTES due to insufficient image data. Thus, hereafter we use the final spot locations calculated from the ATPM offset analysis (Figure 1, left).

#### 2.4. 3D Thermal Model for Particle-coated Boulders

We used the 3D finite element (FE) thermal model from Ryan et al. (2020, 2022) to investigate the thermal effects of thin particle coatings on rocks at the Nightingale sample site. The model calculates the kinetic temperature and brightness temperature spectrum across all OTES wavelengths of a rock substrate covered in spherical particles. We varied the particle sizes and the material properties (thermal conductivity, density, and heat capacity) of the particles and substrate. The results of this model were compared to a simple 1D thermal model with constant material properties with depth, like the one that is applied to each facet of the ATPM. We fit the 3D model results using the 1D model as a look-up table, much in the same way that the OTES data are fit against the ATPM model look-up tables, to calculate apparent thermal inertia values of different particle-coated rock configurations. This approach is similar to that taken by Biele et al. (2019) in their study of surfaces coated



**Figure 2.** Thermal inertia results from the ATPM using the OTES data from Checkpoint rehearsal, Matchpoint rehearsal, and TAG. The dashed white circle marks the approximate rim of Hokioi Crater. Boxes indicate the locations of Figures 3 and 4.

in thin layers of dust. The model and assumed material properties are described in detail in Appendix A.

### 3. Results and Interpretation

#### 3.1. Thermal Inertia Trends in Hokioi Crater

Figure 2 shows the thermal inertia values calculated by the ATPM using the OTES Checkpoint, Matchpoint, and TAG observations with corrected spot locations. The thermal inertia values are generally higher outside of Hokioi Crater than inside, consistent with previous studies (Rozitis et al. 2020b, 2022; see Figure B5) though with lower values than previously noted in some locations. There are several instances (e.g., Figure 3(a)) of locally elevated thermal inertia values that spatially coincide with rock or rock clusters that appear to be the higher-reflectance lithology described by DellaGiustina et al. (2020) and Rozitis et al. (2020b, 2022) and classified as Type C or D in the scheme of Jawin et al. (2023). Conversely, instances of locally depressed thermal inertia typically coincide with patches of finer regolith and in rarer cases identifiable instances of dark-toned (Type A and/or B) boulders (e.g., Figure 3(b)).

After correcting for systematic OTES spot offsets, we found that observations from the TAG approach intersect or nearly intersect portions of the TAG site (Figures 4 and 5). In particular, the OTES observations obtained during the TAG approach ( $\sim 5$  minutes before surface contact) pass over the two rocks that were eventually contacted by TAGSAM, as described in Lauretta et al. (2022) and Walsh et al. (2022): the  $\sim 40$  cm long plate rock (triangular in shape) that flipped upward like a rigid plate and the  $\sim 20$  cm long tagged rock that may have been partially crushed (Figure 6).

Where the OTES FOV crosses these two rocks, there is a substantial decrease in thermal inertia to values of  $50\text{--}150$  ( $\pm 50$ )  $\text{J m}^{-2} \text{K}^{-1} \text{s}^{-1/2}$  (Figures 4 and 5). This decrease is predicted by the ATPM regardless of which OLA DTM is used

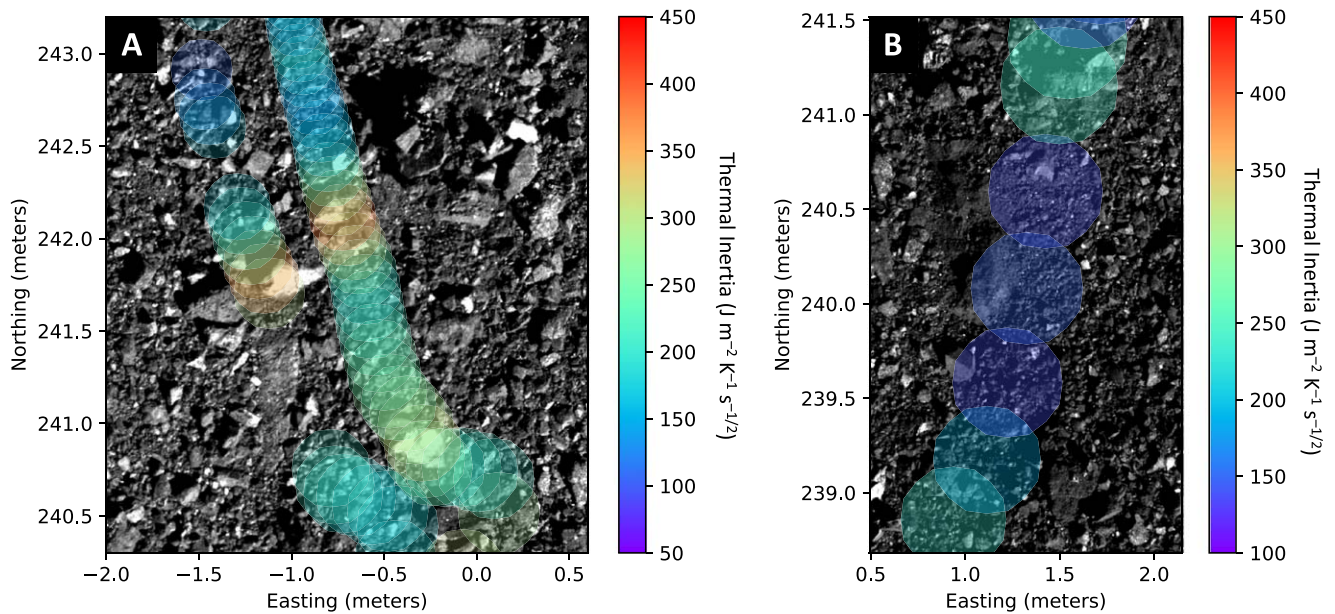
(v20 or v21). The lowest thermal inertia values are found when the OTES FOV is centered on the contact between the two rocks. Based on visual analysis of the stereoscopic images of the site (Figure B6), there appears to be a  $\sim 7$  cm long rock with a flat surface (Figure 6, lower-left arrow) nearly hidden in shadow within a crevice between the plate rock and tagged rock. Also within the crevice is what appears to be an aggregate of smaller particles, though they are difficult to resolve and measure individually. It is possible that these materials within the crevice may be partly or fully responsible for producing the spatially coincident lowest thermal inertia values ( $\lesssim 100 \text{ J m}^{-2} \text{K}^{-1} \text{s}^{-1/2}$ ). However, the thermal inertia values obtained for spots on the two rocks that do not intersect this contact ( $100\text{--}150 \text{ J m}^{-2} \text{K}^{-1} \text{s}^{-1/2}$ ) are still lower than values for the local terrain ( $150\text{--}270 \text{ J m}^{-2} \text{K}^{-1} \text{s}^{-1/2}$ ), suggesting that the low-thermal-inertia signature is at least in part due to the instrument FOV intersecting these rocks.

The plate rock (Figure 6, left outline) is covered in a layer of particles ranging in size from  $\sim 5$  mm to a few centimeters in diameter. The layer is thickest toward the north and tapers out to zero thickness toward the south (from right to left in Figure 6). The uncoated end of the rock clearly has a distinct texture compared to the coated portion, the latter of which was partially observed by OTES. The tagged rock has a distinctly different surface texture from the uncoated portion of the plate rock and appears to have far fewer particles on its surface. Stereoscopic images of the scene (Figure B6) greatly aid in the process of distinguishing perched particles from possible embedded clasts or the inherently hummocky surface of the rock itself. Several larger stones (few centimeters to  $\sim 8$  cm maximum) rest to either side of the tagged rock, while only a few particles are obviously sitting on its surface. One bright  $\sim 3$  cm stone (Figure 6, lower-right arrow) appears to protrude distinctly from the surface of the rock in the stereoscopic images. We conclude that it is resting there and may even have been collected in its entirety by TAGSAM. Other, smaller, bright stone-like features (Figure 6, upper arrow) are too small to determine conclusively whether they are on the surface or embedded. Further supporting evidence for the relative absence of coarse particle coatings is provided by the texture of the rock: It has a dome-like shape that is obvious in the stereoscopic images. The western edge of the rock (top edge in Figure 6) appears to have a nearly vertical slope that would far exceed the angle of repose and thus could not easily host perched particles. The texture of this surface is very similar in appearance to the top surface of the rock, further supporting that it is relatively free of perched particles, with the exception of the few noted in Figure 6. The hummocky surface texture of this rock may however serve to trap and/or mask the presence of millimeter-scale and finer particles.

#### 3.2. Thermal Inertia of Particle-coated Surfaces

The 3D thermal model of particle monolayers reveals that the apparent thermal inertia of rocks on Bennu could be very strongly influenced by the presence of thin coatings of millimeter- to centimeter-scale particles (Figures A1 and 7). For very large particles (5 cm, larger than the diurnal skin depth in all cases), the apparent thermal inertia of the system is near that of the individual particles themselves. As the particle size decreases below that of the diurnal skin depth, the apparent thermal inertia of the system also drops significantly. The thermal properties of the substrate appear to have muted





**Figure 3.** (a) Elevated thermal inertia values in Matchpoint and TAG data correspond spatially with higher-reflectance boulders that are tens of centimeters in size. (b) Low thermal inertia values in Checkpoint data on fine regolith and a dark-toned boulder. In both figure frames, OTES spots are colorized by thermal inertia. We omit two out of every three sequential spots in this figure to improve clarity. The basemap is a PolyCam Recon C mosaic.

influence on apparent thermal inertia across the full range of particle sizes tested (1 mm–5 cm). The thermal properties of the particles themselves, though important when the particles are very large, are also of secondary importance in affecting the apparent thermal inertia of the system. The same overall trends are observed when we fit to nighttime and seven-station data (Figure B7) or when we extract brightness temperature from the 3D model at a different wavelength (here we used 10  $\mu\text{m}$ ).

The 3D model results indicate that low thermal inertia of a particle-coated rock may not be indicative of the properties of the rock itself. Thus, the plate rock could have a higher thermal inertia than indicated by the OTES data (100–150  $\text{J m}^{-2} \text{K}^{-1} \text{s}^{-1/2}$ ). The tagged rock conversely appears to have far fewer particles on its surface and thus may have been less affected by this phenomenon, though we cannot fully eliminate it as a possibility due to the limited availability of high-resolution images.

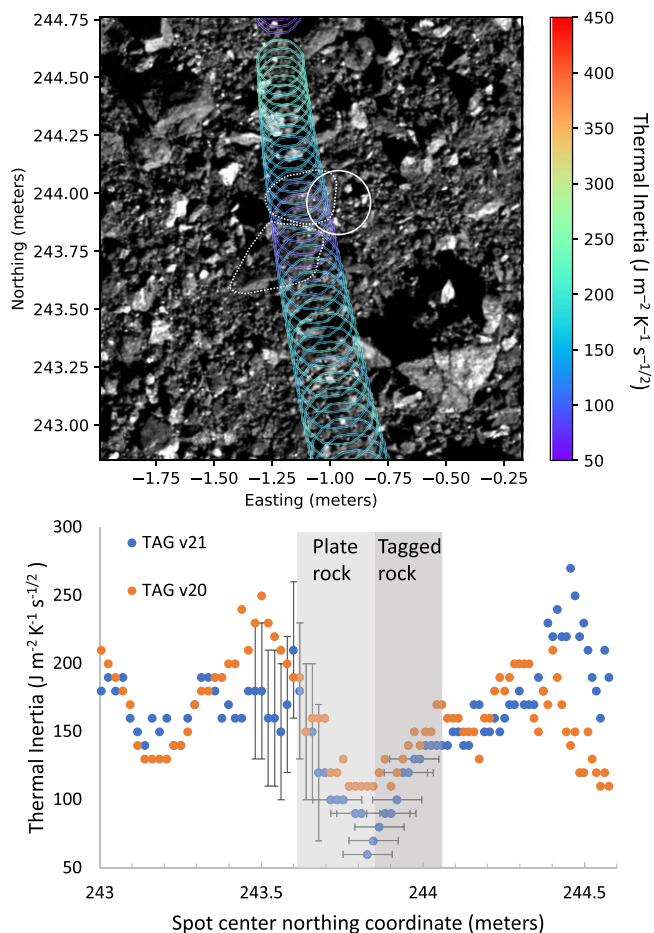
The diurnal temperature curves from the 3D simulations of particle-coated surfaces are also typically distorted compared to those of unlayered models (Figures A2 and B8). These distortions are different from those observed in models of dust-coated surfaces (Biele et al. 2019). First, there is a significant shift in the time at which the peak daytime temperature occurs. For the largest particle coating that we tested (5 cm diameter), the peak time shifts later into the afternoon—so late that it cannot be reasonably fit using peak time alone with an unlayered thermal model without using an unrealistically high thermal inertia value (several thousand  $\text{J m}^{-2} \text{K}^{-1} \text{s}^{-1/2}$ ). As the sphere size decreases, the peak time gradually moves to earlier times, which is similar to what is seen in unlayered model results with decreasing thermal inertia values. The opposite trend is observed in dust-coated models, where a peak temperature time shifts to earlier times of day in the presence of dust coatings (Biele et al. 2019).

The second distortion is in the rate of nighttime cooling. In dust-coated models, nighttime cooling rates are typically reduced (curves are flatter) compared to unlayered models (Biele et al. 2019, their Figure 2). In our model, for each set of

material properties used there is a sphere size threshold above which the nighttime cooling curves are flatter and below which they are steeper as compared to the unlayered 1D model best-fit solution. This size threshold is  $\sim 1$  cm for the cases where the thermal inertia of both spheres and substrate is equal to  $860 \text{ J m}^{-2} \text{K}^{-1} \text{s}^{-1/2}$  or  $300 \text{ J m}^{-2} \text{K}^{-1} \text{s}^{-1/2}$  (Figure 7). The threshold is  $\sim 5$  mm for the cases where the spheres' thermal inertia is  $860 \text{ J m}^{-2} \text{K}^{-1} \text{s}^{-1/2}$  and the substrate's is  $300 \text{ J m}^{-2} \text{K}^{-1} \text{s}^{-1/2}$  or  $150 \text{ J m}^{-2} \text{K}^{-1} \text{s}^{-1/2}$ . The nighttime cooling rates at these sphere size thresholds are reasonably well matched by the unlayered model; however, the overall amplitude of the diurnal temperature curve is not always well matched. We do not attempt to quantify the goodness of fit because in practice the fitting of this type of model to real spacecraft data would depend on the nature of the data. For example, data obtained by the Hayabusa2 Mascot Radiometer (MARA) consist of continuous thermal infrared brightness temperature data, and thus any minor distortions in the cooling curve due to layered scenarios should be easily detectable. The OTES global survey data, on the other hand, consist of data only collected at seven local times (“stations”) in the diurnal cycle. Data interpretation is further complicated by the absence of alignment between the OTES spots from each time station. Thus, the fitting of layered models to these data may allow more room for multiple potential model solutions.

#### 4. Discussion

The thermal inertia values within and immediately surrounding Hokioi Crater have peaks and lows that are not evident in the lower-resolution Recon A and B data sets (Rozitis et al. 2020b, 2022). Most local thermal inertia peaks coincide with the presence of higher-reflectance (Type C and D) rocks, consistent with previous findings that these rocks have higher thermal inertia than Bennu's global average and lower-reflectance rocks (Rozitis et al. 2020b, 2022). Thermal inertia lows within Hokioi Crater appear to coincide with areas devoid of larger rocks, consistent with models and laboratory



**Figure 4.** Top: thermal inertia values for OTES spots near the TAGSAM contact point (white circle, 32 cm diameter) observed during the TAG pass. The dotted lines indicate the approximate extents of the larger plate rock and smaller tagged rock. The OTES spots obtained during the TAG approach are very tightly spaced and have significant overlap. This figure only shows every third spot to avoid clutter. The basemap is a PolyCam Recon C mosaic. Bottom: thermal inertia of the OTES spots in the top figure. The results from running the ATPM model with each of the two DTMs (OLA v20 and v21) are shown for comparison. The approximate extent of the plate rock and the tagged rock are indicated in light gray and dark gray, respectively. Representative error bars (all the same) have been added to some points but not all to avoid clutter. The spot center position error bars indicate the extent of the OTES spot ( $\pm 7.6$  cm based on the OTES spot diameter).

measurements showing a direct relationship between fine-regolith particle size and thermal inertia. In one instance (Figure 3(b)), a series of low-thermal-inertia observations ( $100\text{--}110 \text{ J m}^{-2} \text{ K}^{-1} \text{ s}^{-1/2}$ ) on fine regolith partially overlap a partly buried, dark-toned (Type A or B) rock. The thermal signature appears to be unaffected by the presence of this rock, given that the thermal inertia is unchanging as the rock enters and then exits the OTES FOV in consecutive observations. This suggests that the rock and fine regolith have similar thermal inertia values.

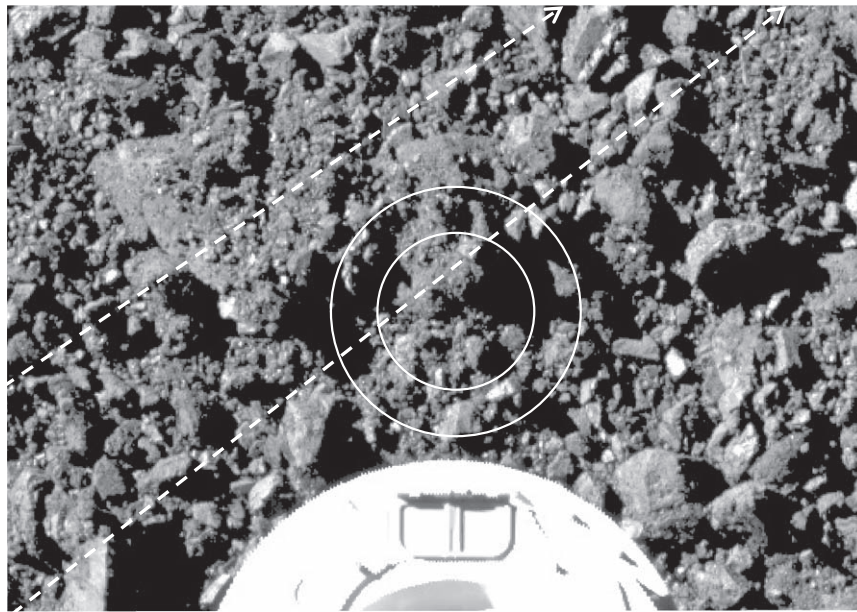
The thermal inertias of the two rocks contacted by TAGSAM ( $100\text{--}150 \text{ J m}^{-2} \text{ K}^{-1} \text{ s}^{-1/2}$ ) are lower than any values yielded by thermal analysis of other mission phase data. The 40 cm plate rock (Figure 6, left outline) is covered in particles ranging from at least millimeters to centimeters in size, and we found that coatings like this could significantly reduce the apparent thermal inertia, essentially masking the substrate properties. The cantilever-like response of this rock to

TAGSAM contact suggests that it is not extremely friable and thus may have a higher true thermal inertia that is masked by the particle coating. The plate-like form also suggests that it may be a Type C or D boulder, which tend to have higher thermal inertia, higher strength, and higher albedo (possibly darkened by dust and particles here) than the darker and more rugged Type A and B boulders. Although this rock was shifted during TAG—either due to direct contact between a shadowed or otherwise obscured portion of the rock and TAGSAM, or indirectly via TAGSAM-induced movement of other surrounding rocks—it was not below the TAGSAM sampling aperture and is unlikely to have been sampled.

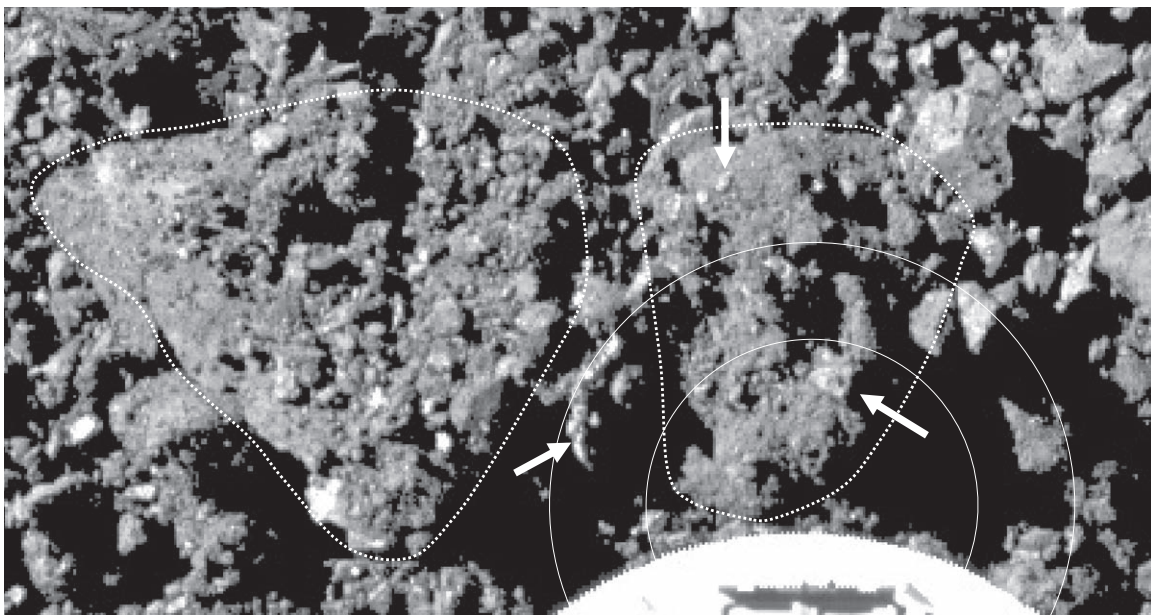
Conversely, the 20 cm tagged rock (Figure 6, right outline) appears to have only a few perched particles, far fewer than its neighbor; this is most obviously seen in the stereoscopic images (Figure B6). It furthermore does not appear to be coated in thick dust, which could also suppress apparent thermal inertia. According to Figure 4 of Biele et al. (2019), a continuous dust coating approximately 0.5–2 mm thick would be required to reduce the apparent thermal inertia of a rock from a true value of  $300\text{--}1200 \text{ J m}^{-2} \text{ K}^{-1} \text{ s}^{-1/2}$  to the mid-range value of  $100 \text{ J m}^{-2} \text{ K}^{-1} \text{ s}^{-1/2}$  observed for the tagged rock. We see no visual evidence for dust coatings of this thickness on the tagged rock in Figure 6. We cannot completely rule out thinner dust coatings that are difficult to detect by eye, nor coatings with small areal abundance (e.g., filling small local depressions or cracks). Nearly all OTES spectra of Bennu contain evidence of thin ( $5\text{--}10 \mu\text{m}$ ) and/or patchy coatings of dust (Hamilton et al. 2021). Nevertheless, their effect on apparent thermal inertia would be small—Rozitis et al. (2020b) found that continuous thin layers of dust ( $<50 \mu\text{m}$ ) and 10% areal coverage of thicker dust only result in a roughly  $10 \text{ J m}^{-2} \text{ K}^{-1} \text{ s}^{-1/2}$  change in the apparent thermal inertia of a rock.

The tagged rock has the hummocky surface texture typical of other rough, low-reflectance, low-thermal-inertia rocks (Types A and B) observed on Bennu, including the partly buried rock among fine regolith (Figure 3(b)) described above. Given that the low-reflectance rock type is the most common on Bennu, it is not surprising to find potentially representative examples at and near the TAG site. The tagged rock has a thermal inertia ( $100\text{--}150 \text{ J m}^{-2} \text{ K}^{-1} \text{ s}^{-1/2}$ ) that is somewhat lower than other low-reflectance rocks analyzed to date ( $180\text{--}400 \text{ J m}^{-2} \text{ K}^{-1} \text{ s}^{-1/2}$ ). The difference may simply be due to the smaller observational footprint used here compared to previous studies, where larger footprints would have resulted in the muting of high- and low-thermal-inertia signatures due to spatial averaging. Previous studies have shown that the low-reflectance rocks could have a wide range of thermal inertia values (Rozitis et al. 2020b, 2022). This may indicate a range of weathering states, though the relationship between thermal inertia and degree of weathering may be complicated. Some weathering processes (e.g., thermal fracturing) would work to decrease thermal inertia, while others (e.g., micrometeorite impact compaction) could increase thermal inertia by collapsing pores and densifying the rock (Rozitis et al. 2020b). There may also exist a range of inherent compositional differences that are responsible for the range of thermal inertia values. For example, assuming a simple two-component breccia consisting of higher-thermal-inertia clasts embedded in a lower-thermal-inertia matrix, there may be a range of clast-to-matrix ratios or clast and matrix thermophysical properties that would affect the bulk rock’s thermal inertia (e.g.,





**Figure 5.** SamCam image taken approximately 30 s before TAGSAM contact with the surface. The front edge of TAGSAM can be seen at the bottom of the frame. The lateral extent of the OTES data swath that was collected during the TAG approach is shown as dashed lines, with arrows indicating the direction of data collection (compare to Figure 4, top). The larger white circle indicates approximately where the 32 cm diameter TAGSAM touched the surface. The smaller white circle indicates the extent of the TAGSAM opening. Regolith within the inner circle may have been sampled in bulk. Smaller particles from within the annular area between the two circles may have been sampled by the contact pads. North is approximately toward the right. SamCam image 20201020T214918S448\_sam\_iofL2pan5.

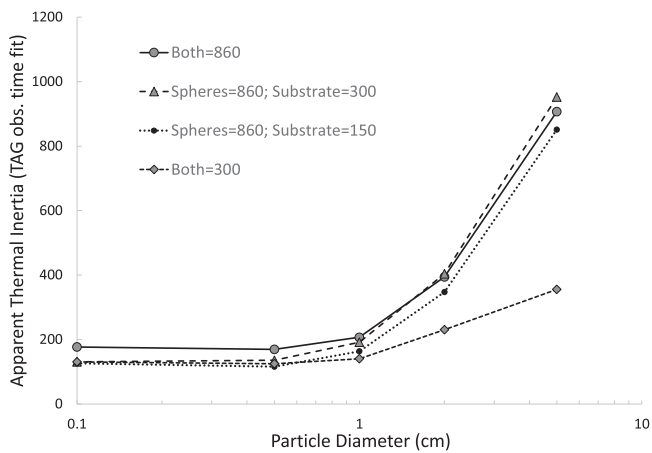


**Figure 6.** Highest-resolution unobstructed view of the two rocks that were moved and possibly modified by the TAG event—“plate rock” (left outline) and “tagged rock” (right outline). Arrows point to stones described in the main text. The upper arrow points to a stone that is  $\sim 1$  cm in length. The lower-right arrow indicates a stone  $\sim 3$  cm in length. The lower-left arrow points to a longer, flat stone  $\sim 7$  cm in length. As in Figure 5, the larger circle indicates the outer extent of the TAGSAM head (32 cm diameter). The smaller circle indicates the extent of the opening in TAGSAM through which regolith particles may have been ingested. North is approximately toward the right in the image. SamCam image 20201020T214934S275\_sam\_iofL2pan5.

Rozitis et al. 2022). The tagged rock may therefore exist near the low end of a range of thermal inertias among the low-reflectance rocks, meaning that it could be more or less weathered (depending on the dominant process) and/or contain fewer breccia clasts than other low-reflectance boulders on Bennu.

On asteroid Ryugu, the Hayabusa2 Mascot lander instrument suite, including MARA, observed a rock with a similar appearance at a comparable spatial scale. This rock was found to have a thermal inertia ( $\sim 250\text{--}280 \text{ J m}^{-2} \text{ K}^{-1} \text{ s}^{-1/2}$ ; Grott

et al. 2019; Hamm et al. 2022) that is very similar to values obtained from orbit (Sugita et al. 2019; Shimaki et al. 2020) and somewhat higher than the tagged rock. The presence of all but a very small amount of dust ( $\leq 3\%$  spatial coverage) was ruled out by thermal models (Grott et al. 2019; Hamm et al. 2023). Rather, similar to Bennu’s low-reflectance boulders, the thermal inertia of Ryugu’s boulders has been attributed to an internal porosity of 30%–52% (Grott et al. 2019; Hamm et al. 2020)—potentially much higher than



**Figure 7.** Modeled apparent thermal inertia of a rock covered with a continuous monolayer of spherical particles. The unlayered thermal model was fit to the 3D model radiance at local hour 14:40, the approximate time that OTES observed the eventual TAG point as the spacecraft approached the surface for sample collection. Particle sizes are 1 mm, 5 mm, 1 cm, 2 cm, and 5 cm. The thermal inertia of the individual particles, the rock substrate, or in some cases both sets of materials are indicated in the legend (units of  $\text{J m}^{-2} \text{K}^{-1} \text{s}^{-1/2}$ ).

any measured meteorite analog (Flynn et al. 2018; Opeil et al. 2020), which could be indicative of low strength and high friability.

Ryugu also hosts rare boulders with much lower thermal inertia values that are more consistent with the tagged rock's. These low-reflectance boulders, present in the centers of fresh craters, have thermal inertias of  $\sim 50\text{--}70 \text{ J m}^{-2} \text{K}^{-1} \text{s}^{-1/2}$ , which Sakatani et al. (2021) attribute to extremely high porosity ( $>70\%$ ). They interpret these boulders as minimally processed remnants of the uppermost part of a partially consolidated layer on Ryugu's parent body. The resolution of images of these boulders differs substantially from those of the tagged rock, so we cannot confidently assess their morphologic similarity. Nevertheless, the low thermal inertia values that we obtained could likewise be indicative of very high porosity and perhaps a similar parent body provenance.

Recent results from the analysis of Hayabusa2 samples conflict with remote-sensing-based thermal inertias and derived sample properties. Although remote-sensing observations of Ryugu indicated thermal inertia values in the range of approximately  $200\text{--}300 \text{ J m}^{-2} \text{K}^{-1} \text{s}^{-1/2}$  (Grott et al. 2019; Sugita et al. 2019; Shimaki et al. 2020), returned samples have been measured to have a thermal inertia values about  $800\text{--}1250 \text{ J m}^{-2} \text{K}^{-1} \text{s}^{-1/2}$  (Nakamura et al. 2022; Ishizaki et al. 2023). Although porosity was not directly measured, the bulk density of Hayabusa2 samples ( $1.7\text{--}1.9 \text{ g cm}^{-3}$ ; Nakamura et al. 2022) is similar to some measured CI, CM, and ungrouped CC meteorites (Macke et al. 2011). This can be converted to an approximate porosity of  $20\%\text{--}30\%$  (assuming a CI grain density of  $2.42 \text{ g cm}^{-3}$ ; Macke et al. 2011), which is lower than remote-sensing predictions.

We consider two explanations for the discrepancy between remote sensing and sample measurements of thermal and physical properties, with the aim of preparing for a possibly similar scenario with the Bennu samples. First, the length scales at which the boulders and returned samples were probed differ substantially. Remote-sensing-based thermal inertia values are sensitive to material properties within the upper few diurnal thermal skin depths, translating to length scales on

the order of about  $5\text{--}20 \text{ cm}$ . In contrast, direct sample measurements are sensitive to length scales based on the size of the sample and the specifics of the measurement technique. The thermal diffusivity of Ryugu samples was measured at length scales on the order of only hundreds of micrometers. Those measurements may therefore be closer to sampling the grain thermal inertia rather than a rock thermal inertia.

Second, the actual sampling event may have selectively retrieved samples of a particular type or may have processed them. The Hayabusa2 sampling mechanism, a bullet fired into the surface, was highly energetic and could have fractured rocks along planes of preexisting weakness that could previously have served to reduce apparent thermal inertia. The OSIRIS-REx sampling mechanism was less energetic, though forces during the entry, descent, and landing (EDL) of the sample capsule may have been sufficient to disaggregate some particles.

Both possible explanations are discussed by Ishizaki et al. (2023), who showed that thermal fracture networks may be responsible for reducing the apparent thermal inertia of the rocks on Ryugu. They observed small cracks in Ryugu samples and speculated that a network of larger-scale and more widely developed cracks may be present in Ryugu's boulders, with spacing lengths greater than those in the samples (up to hundreds of micrometers) but smaller than the diurnal thermal skin depth ( $\sim 2 \text{ cm}$ ). The energetic nature of the Hayabusa2 sampling may have fractured rocks along the larger-scale crack network, resulting in smaller sample pieces that are less heavily fractured and thus biased toward having a higher thermal inertia. Elder (2024) modeled a substantial reduction in apparent thermal inertia via diurnal simulations of Bennu with fractures just beneath the surface.

Brecciation within Bennu's and Ryugu's boulders may also result in thermal properties that scale with sample size. Breccia clasts may be bound together in these boulders by a porous matrix, which would have a similar effect as fracture networks on bulk thermal conductivity. If the predominant breccia clast size is smaller than the thermal wave ( $\sim 2 \text{ cm}$ ) but larger than the length scale of sample measurements, then direct measurements of thermal properties would be biased toward the higher value of the individual breccia clasts. The boulders of Bennu and Ryugu may preferentially fragment along the breccia clast boundaries when naturally weathered by thermal fracturing and meteoroid bombardment and when energetically sampled or agitated during sample return. In such a case, the breccia clasts themselves are found in the final sample aggregate, while the information about how the clasts were connected and behaved thermally and physically together could be lost.

The OSIRIS-REx returned sample may contain many millimeter- to centimeter-scale particles that would allow for the examination of thermal properties and internal structure across a larger range of spatial scales than permitted by the smaller Hayabusa2 samples. Preliminary sample measurements in the OSIRIS-REx curation environment, including structured light scanning, gas pycnometry, and X-ray computed tomography, will be used to identify samples with a wide range of bulk density and porosity values and particles with possible brecciation for further detailed measurement (Lauretta et al. 2023a). Coordinated mapping of internal structural characteristics (e.g., void and fracture networks, breccia clast size and context), coupled with multi-scale strength and



thermal conductivity measurements, will help to constrain models for the multi-scale thermal and physical properties of asteroid Bennu.

## 5. Conclusions

We analyzed high-resolution thermal emission data collected by the OSIRIS-REx spacecraft during close-proximity observations of the sample-collection site in Hokioi Crater on Bennu. After correcting the pointing of these observations to accurately overlay them on high-resolution images, we calculated thermal inertia using a high-resolution thermal model. We found higher thermal inertias for observations that intersect some high-reflectance rocks, consistent with previous findings that these rocks have a higher thermal inertia than particulate regolith and low-reflectance boulders on Bennu. Local thermal inertia lows conversely tend to coincide with patches of fine regolith and in a few cases dark-toned boulders.

We found a distinct, very low thermal inertia ( $100\text{--}150 \text{ J m}^{-2} \text{ K}^{-1} \text{ s}^{-1/2}$ ) associated with two rocks that were contacted by the spacecraft's sampling device. Previous analyses showed that one responded to contact like a rigid plate, whereas the other appears to have been partially crushed—and thus potentially sampled—even though the contact forces were minimal. The rigid plate rock was coated in sand-to pebble-sized particles, which our 3D thermal model showed could artificially suppress the measured thermal inertia below that of the solid rock substrate or the particles themselves. This masking effect is not very sensitive to the substrate properties. Thus, particle coating could be responsible for the apparent very low thermal inertia of this rock.

The rock that was partially crushed, however, did not have obvious particle or dust coatings, suggesting that the model-derived thermal inertia value is indicative of its true material properties. This rock may have a high degree of internal porosity, as has been posited for other low-thermal-inertia boulders on Bennu and Ryugu. However, remote-sensing-based predictions of high-porosity materials on Ryugu have not been borne out by Ryugu sample analysis. Consequently, we approach the interpretation of thermal inertia in relation to overall porosity with caution. The length scale of sample analysis may critically affect the measured properties, particularly if large fracture networks, acting as thermal resistors, exist within boulders at centimeter and larger scales but are underrepresented in millimeter and finer-scale samples. Additionally, the forces on the sample during sampling and EDL may alter the physical and thermal properties via particle breakage along major preexisting fractures or breccia clast boundaries.

We recommend searching for pieces of this rock on the basis of morphology and density during preliminary examination of the OSIRIS-REx sample, though it may be difficult to recognize if it was heavily comminuted during sample capsule EDL. Measurement of void, fracture, and breccia clast characteristics and thermal properties will help us to better understand remotely derived thermal inertia values and the link between thermal and physical properties.

## Acknowledgments

This material is based on work supported by NASA under contract NNM10AA11C issued through the New Frontiers Program. A.J.R. acknowledges the support of NASA grant Nos. 80NSSC21K0146, 80NSSC21K0827 and 80NSSC21K1805.

B.R. acknowledges funding support from the UK Science and Technology Facilities Council (STFC). D.P.M., M.B., and M.D. acknowledge the support of the French space agency CNES. M. D. also acknowledges support from the ANR “ORIGINS” (ANR18-CE31-0014). C.E. acknowledges the support of the OSIRIS-REx Participating Scientist Program. C.E.’s contribution was carried out at the Jet Propulsion Laboratory, California Institute of Technology, under a contract with the National Aeronautics and Space Administration. We thank two anonymous reviewers for constructive feedback that improved the quality of this manuscript. We are grateful to the entire OSIRIS-REx team for making the encounter with Bennu possible.

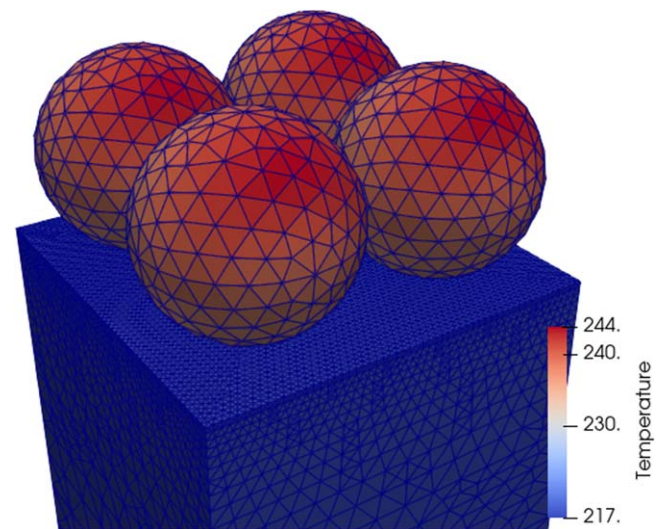
## Data Availability

The OTES data used in this work can be found at [https://sbn.psi.edu/pds/resource/doi/orex\\_otes\\_11.0.html](https://sbn.psi.edu/pds/resource/doi/orex_otes_11.0.html) (Christensen et al. 2019). Model outputs and code used in this work are available in Ryan et al. (2024).

## Appendix A

### 3D Finite Element Model of Particle-coated Surfaces

The 3D model FE formulation is based on an implicit diffusion equation solver and an explicit surface-to-surface radiative heat transfer solver, which were integrated upon Cimlib, a C++ scientific FE library (Dignonnet et al. 2007). We approximate a particle monolayer as spheres of uniform diameter packed in a square pattern on a flat rock substrate that extends below the subsurface to a depth of at least 12 diurnal thermal skin depths (Figure A1). Surface-to-surface radiative heat transfer is periodic in the lateral directions, which allows us to use a small representative volume element consisting of a  $2 \times 2$  arrangement of spheres on the flat rock substrate. This geometry was converted to a tetrahedral mesh in COMSOL Multiphysics. We utilized the same tetrahedral mesh geometry for all simulations by simply adjusting a scaling parameter in our thermal model. The maximum size of elements within the spheres and within the uppermost surface of the rock substrate was set so that the largest ratio of element



**Figure A1.** Geometry and example temperature result for the 3D thermal model of particle monolayers on a rock substrate. In this example, the spheres are 5 cm in diameter, the thermal inertia of both materials is  $860 \text{ J m}^{-2} \text{ K}^{-1} \text{ s}^{-1/2}$ , and the time of observation is local noon.

size to diurnal skin depth is 0.2. Mesh element size increases with depth in the rock substrate by a factor of 1.15 (as in the rigorously validated thermal model of Kieffer et al. 2013). To verify that our mesh resolution is satisfactory, we doubled the mesh element count within the spheres and within each layer of the substrate and recomputed a simulation where the ratio of mesh element size to diurnal skin depth was largest (the worst-case scenario). The maximum brightness temperature difference compared to the coarser model result was only 0.15 K. This is satisfactory for this work, given that the model parameters that we vary (e.g., sphere diameter) result in brightness temperature changes of at least several kelvin.

The edges of the rock substrate that extend into the subsurface are assigned an insulating (zero heat flux) boundary condition. The upper surface of the rock substrate and all surfaces of the spherical particles are allowed to participate in surface-to-surface radiative heat transfer, heat loss to space, and heating by a solar source at an infinite distance. Rays are traced between all triangular surface elements with the Intel Embree ray-tracing library to determine visibility. During this ray-tracing and subsequent view factor calculation step, lateral periodicity is taken into account by duplicating the geometry in the  $\pm X$ - and  $\pm Y$ -directions (where  $Z$  is pointing upward toward space) to a distance of two periodic distances. As such, the geometry is copied nine times to make the first layer of periodicity and 16 times to make a second layer of periodicity. View factors for all elements that share direct line of sight, via the ray tracing, are calculated using a single line integration method (Mitalas & Stephenson 1966). The ray tracing is also used to determine which surface mesh elements should be visible to a solar source. Rays are traced from the center of each mesh element in the direction of the solar source, again taking periodicity into account by duplicating the geometry. If the ray does not intersect another mesh element after two layers of periodic geometry duplication, then the element from which the ray originated is assumed to be fully illuminated by the Sun.

The model assumes that all heat transfer between the particles and the substrate is accomplished radiatively. The particles are thus not touching the surface of the substrate in the model, eliminating the need for computationally expensive heat transfer through the very narrow contacts. We consider this to be a satisfactory assumption given that the contacts between irregular particles are known to be extremely restrictive to heat flow (e.g., Sakatani et al. 2018; Persson & Biele 2022). For particles larger than about 5 mm, radiative heat transfer is greater than an order of magnitude larger than heat transfer via contact conduction (Ryan et al. 2020). In our model cases with the smallest particles (1 mm), the ratio of radiative conduction to contact conduction is  $\sim 2$ , and thus there may be a small but important contribution that we are ignoring. We expect that this would create a small upturn in the effective surface thermal inertia (Figure 7) moving toward smaller and smaller monolayer particle sizes. This upturn is intuitive and expected, given that an exceptionally fine particle monolayer (e.g., composed of micrometer-scale dust) should have a minimal effect on the effective thermal properties of the surface. Although our assumption of zero contact conduction causes us to lose this upturn in our results for particle sizes smaller than 5 mm, this does not affect our overall interpretation of the results.

Given that this model is meant to be used to interpret thermal inertia values obtained with the ATPM rather than for the direct fitting of OTES data, we approximated a few input parameters

to simplify the implementation and interpretation of the model. Notably, we rounded the length of the Bennu day to 15,450 s and rounded the axial tilt to  $180^\circ$ . We also assumed that all surfaces have an emissivity of unity and an albedo of zero so that multiple ray reflections need not be calculated. Every time step, the position of the Sun was recalculated and ray tracing repeated to determine which surface elements were illuminated. At the start of a run, all elements were initialized at a temperature of 220 K, which we found to be a good depth equilibrium temperature for the given orbital parameters. At the end of each diurnal cycle, model convergence was checked by calculating the model's energy conservation fraction, as in Rozitis & Green (2011). If the ratio of energy emitted and absorbed by all surface mesh elements from the preceding diurnal cycle was  $>0.975$ , the model was considered converged. For most simulations, this took about 10 diurnal cycles. We tested running for longer than this and found that the brightness temperatures did not further evolve by more than 1 K. Once convergence is reached, the model executes one final diurnal cycle during which time 60 output files of surface mesh element temperature are written in regular time intervals.

We varied the size of the particles and the material properties of both the particles and substrate according to Table A1. Three sets of material properties were used to give the particle and substrate thermal inertia values of 860, 300, and  $150 \text{ J m}^{-2} \text{ K}^{-1} \text{ s}^{-1/2}$ . The thermal inertia  $860 \text{ J m}^{-2} \text{ K}^{-1} \text{ s}^{-1/2}$  values are based on measurements of samples of asteroid Ryugu returned by Hayabusa2 (Nakamura et al. 2022). The thermal inertia  $300 \text{ J m}^{-2} \text{ K}^{-1} \text{ s}^{-1/2}$  values are based on Bennu's global average thermal inertia (Rozitis et al. 2020b) with the same heat capacity of the Ryugu sample ( $825 \text{ J kg}^{-1} \text{ K}^{-1}$ ) and density and thermal conductivity calculated based on the relationship between meteorite porosity and density from Flynn et al. (2018), assuming a grain density of  $2920 \text{ kg m}^{-3}$ . Finally, the thermal inertia  $150 \text{ J m}^{-2} \text{ K}^{-1} \text{ s}^{-1/2}$  values are meant to approximately represent a very-low-conductivity rock or a dust-coated surface.

**Table A1**  
3D FE Model Parameters

Global Parameters	
Rotation rate	15,450 s (Bennu = 15465.8 s)
Solar range	1.35 au
Latitude	$55.9^\circ$
Axial tilt	$180^\circ$ (Bennu = $177.6^\circ$ )
Observational parameters:	
Observation emission angle	$11.72^\circ$
Observation azimuth angle	$-8.42^\circ$
Observation local solar time	14:40
Model material properties:	
Particle sizes	0.1, 0.5, 1.0, 2.0, 5.0 cm
Thermal conductivity (TI = 860)	$0.5 \text{ W m}^{-1} \text{ K}^{-1}$
Heat capacity (TI = 860)	$825 \text{ J kg}^{-1} \text{ K}^{-1}$
Density (TI = 860)	$1790 \text{ kg m}^{-3}$
Thermal conductivity (TI = 300)	$0.085 \text{ W m}^{-1} \text{ K}^{-1}$
Heat capacity (TI = 300)	$825 \text{ J kg}^{-1} \text{ K}^{-1}$
Density (TI = 300)	$1288 \text{ kg m}^{-3}$
Thermal conductivity (TI = 150)	$0.015 \text{ W m}^{-1} \text{ K}^{-1}$
Heat capacity (TI = 150)	$825 \text{ J kg}^{-1} \text{ K}^{-1}$
Density (TI = 150)	$1790 \text{ kg m}^{-3}$

**Note.** The azimuth angle convention is where  $0^\circ$  is pointed to east ( $+x$ -direction in model with  $\tau$  as the surface normal) and the angle increases counterclockwise. Thermal inertia (TI) values are given in SI units of  $\text{J m}^{-2} \text{ K}^{-1} \text{ s}^{-1/2}$ .



Although assuming a low thermal inertia like this will not perfectly capture the true diurnal thermal behavior of a dust-coated surface (see Biele et al. 2019), we consider it a suitable first-order approximation to examine the effects of a substrate with a very low thermal inertia due to dust.

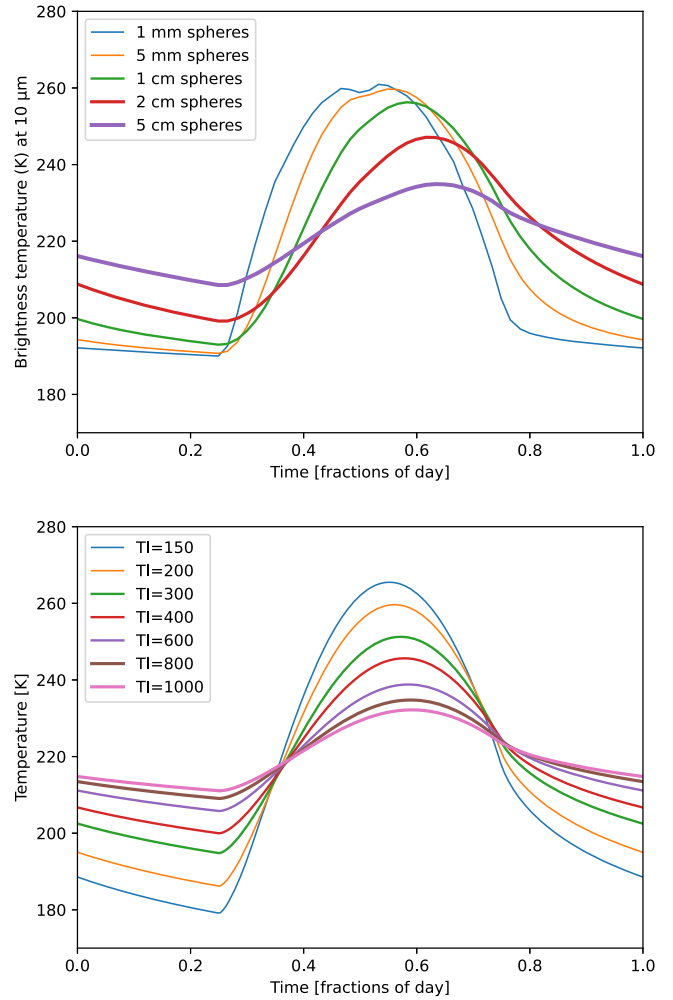
The apparent radiance and brightness temperature of the model output is dependent on viewing conditions, given the 3D nature of the model. We utilize the viewing conditions of the OSIRIS-REx spacecraft at the approximate moment that the OTES instrument observed the TAG site (UTC 2020 October 20 21:44:38). Emission angle, azimuth angle, and local solar time were calculated using the Spice Kernels and the SpicePy Python wrapper for the NAIF C SPICE Toolkit (Annex et al. 2020). The same ray-tracing routine for calculating solar illumination was used to determine which elements of the model should be visible to the spacecraft based on these viewing conditions. For all surface elements that are visible to the spacecraft, the observed radiance was calculated as

$$I(\lambda) = \frac{\sum_{i=1}^N BB(\lambda, T_i) a_i \cos \theta_i}{\sum_{i=1}^N a_i \cos \theta_i},$$

where  $BB$  is a blackbody radiance spectrum calculated from the Planck function with model temperature  $T$  of mesh element  $I$  (of  $N$  elements that are visible to the spacecraft),  $a$  is the area of the mesh element, and  $\theta$  is the observation angle measured relative to the facet surface normal. The resulting radiance spectrum can easily be converted to a brightness temperature spectrum using the Planck function (Figure A2, top).

We ran a simple 1D FE thermal model in COMSOL Multiphysics for comparison to the 3D model results described above. The same model parameters described in the 3D model (rotation rate, solar range, emissivity, etc.) were used in this model to compute incoming solar flux onto a flat surface with material properties that are unchanging with depth. This is functionally equivalent to the 1D model that is computed for each facet in the ATPM. With this model, we generated a look-up table of diurnal surface temperature curves as a function of thermal inertia (Figure A2, bottom).

We follow the model-fitting approach of Biele et al. (2019), who fit a 1D thermal model with uniform material properties (unlayered) to a more complex, dust-layered 1D model. They discuss several methods for best-fitting the results of the more complex model to the uniform properties model, including fitting to the time lag of the peak daytime temperature, fitting maximum and/or minimum temperatures, and least-squares fitting to multiple times throughout the diurnal curve. In our case, we are interested in interpreting ATPM-derived thermal inertia values that were calculated using individual OTES observations at or near the TAG site at local solar afternoon. The ATPM was fit to OTES observations obtained at a single local solar time, as opposed to previous works where overlapping data allowed for fitting at multiple solar times (e.g., Rozitis et al. 2020b; Cambioni et al. 2021). So, to interpret the meaning of this thermal value, it is appropriate to fit the 1D model to our 3D model at that same local solar time as the OTES observations of interest. We use a time of 14:40 based on the local solar time of the OTES TAG site observations. The apparent thermal inertia was thus determined by inputting the brightness temperature of the 3D model at 14:40 into an interpolation of the 1D model brightness temperature at 14:40 versus thermal inertia. Given that the 1D model produces a wavelength-independent kinetic

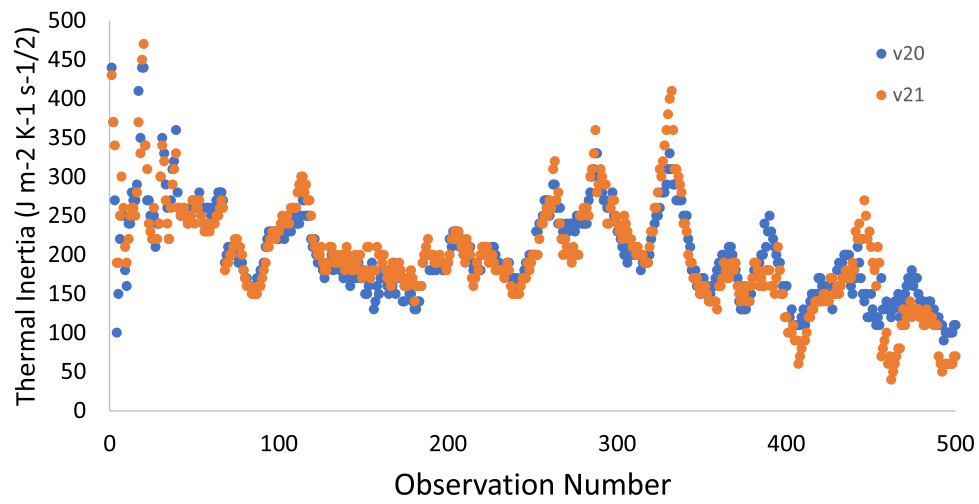


**Figure A2.** Diurnal brightness temperature results from (top) the 3D sphere-coated model as a function of sphere diameter, where both sphere and substrate thermal inertia is fixed  $860 \text{ J m}^{-2} \text{ K}^{-1} \text{ s}^{-1/2}$ , and (bottom) the simple 1D unlayered model as a function of thermal inertia (TI, units  $\text{J m}^{-2} \text{ K}^{-1} \text{ s}^{-1/2}$ ).

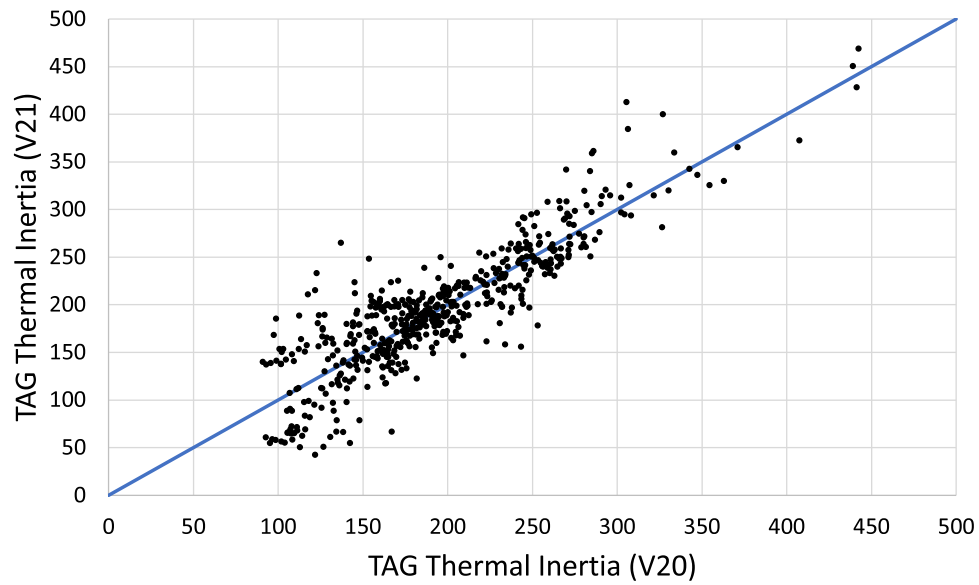
temperature whereas the 3D model produces a brightness temperature spectrum, the user must specify the wavelength at which the 3D model brightness temperature is extracted for the fitting process. We explored the effects of choosing different wavelengths but nominally use  $10 \mu\text{m}$  given that it is near the peak of the Planck thermal emission spectrum at the observed temperatures and is near the middle of the wavelength range used for several other infrared instruments for planetary science (e.g., Grott et al. 2017; Okada et al. 2017). We also explored other fitting options to examine their effect on the resulting apparent TI (see Biele et al. 2019). This includes performing a least-squares fit to seven local times of day corresponding to the seven equatorial stations of the global Detailed Survey phase of the mission (3:20, 6:00, 10:00, 12:30, 15:00, 18:00, 20:40; Figure B7, bottom) and fitting to a nighttime-only observation (3:20; Figure B7, top). The overall trends in the results were not strongly affected by the fitting method.

## Appendix B Supplemental Figures

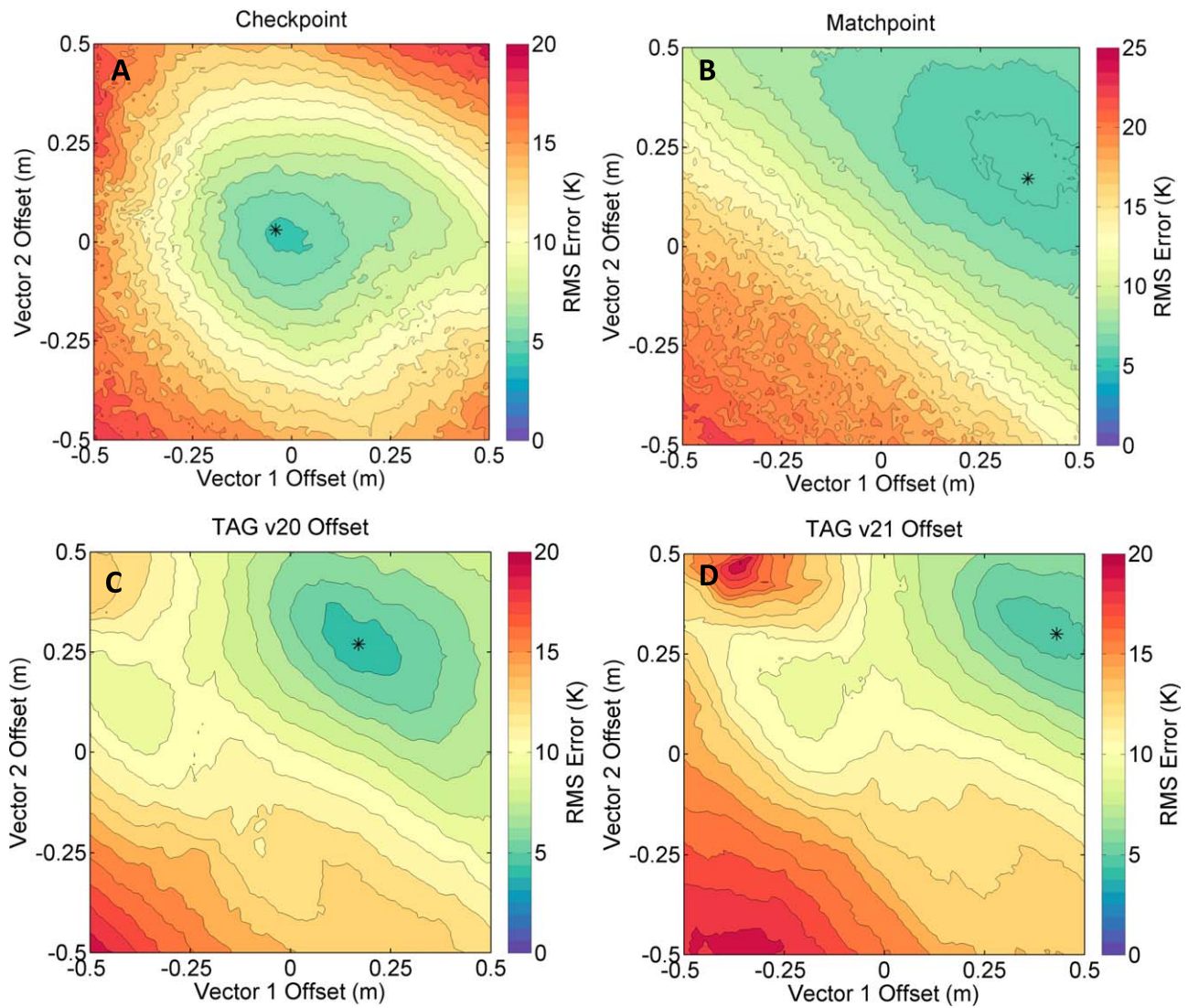
Figures B1–B8 serve as a supplement to the main text.



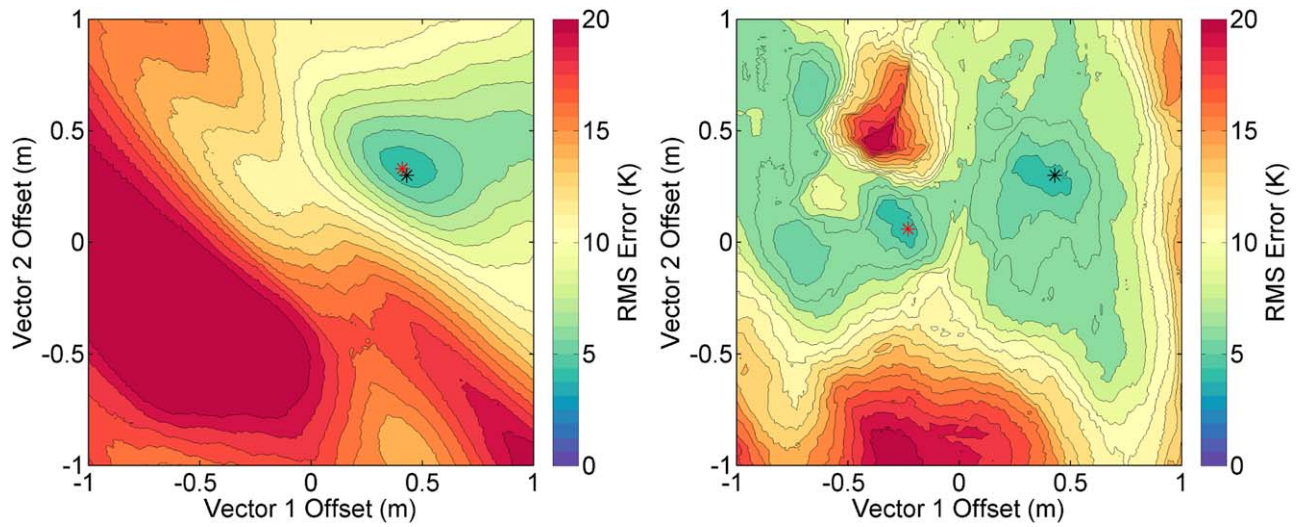
**Figure B1.** Comparison of v20 and v21 DTM model results, shown through time (observation number).



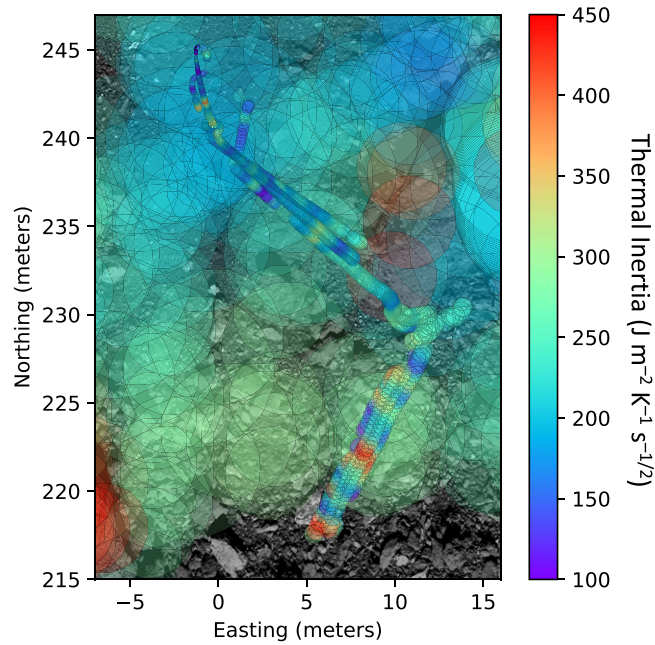
**Figure B2.** Scatter plot comparison between v20 and v21 thermal inertia results. Some random Gaussian noise was added to the thermal inertia values ( $\pm 5$  standard units) to reduce the number of overlapping points for ease of data visualization. Blue line is 1:1 for comparison.



**Figure B3.** Results of OTES spot offset analysis. The rms error was calculated between ATPM  $9.24 \mu\text{m}$  brightness temperatures (assuming a constant mean thermal inertia value) and OTES  $9.24 \mu\text{m}$  brightness temperatures for the Checkpoint (A), Matchpoint (B), and TAG (C–F) data sets. The location of lowest rms error is shown with the black asterisk in each frame. Figures C and D compare results using the OLA v20 and v21 DTMs, with the best solution offset in different locations as expected due to the known offset between the DTMs.

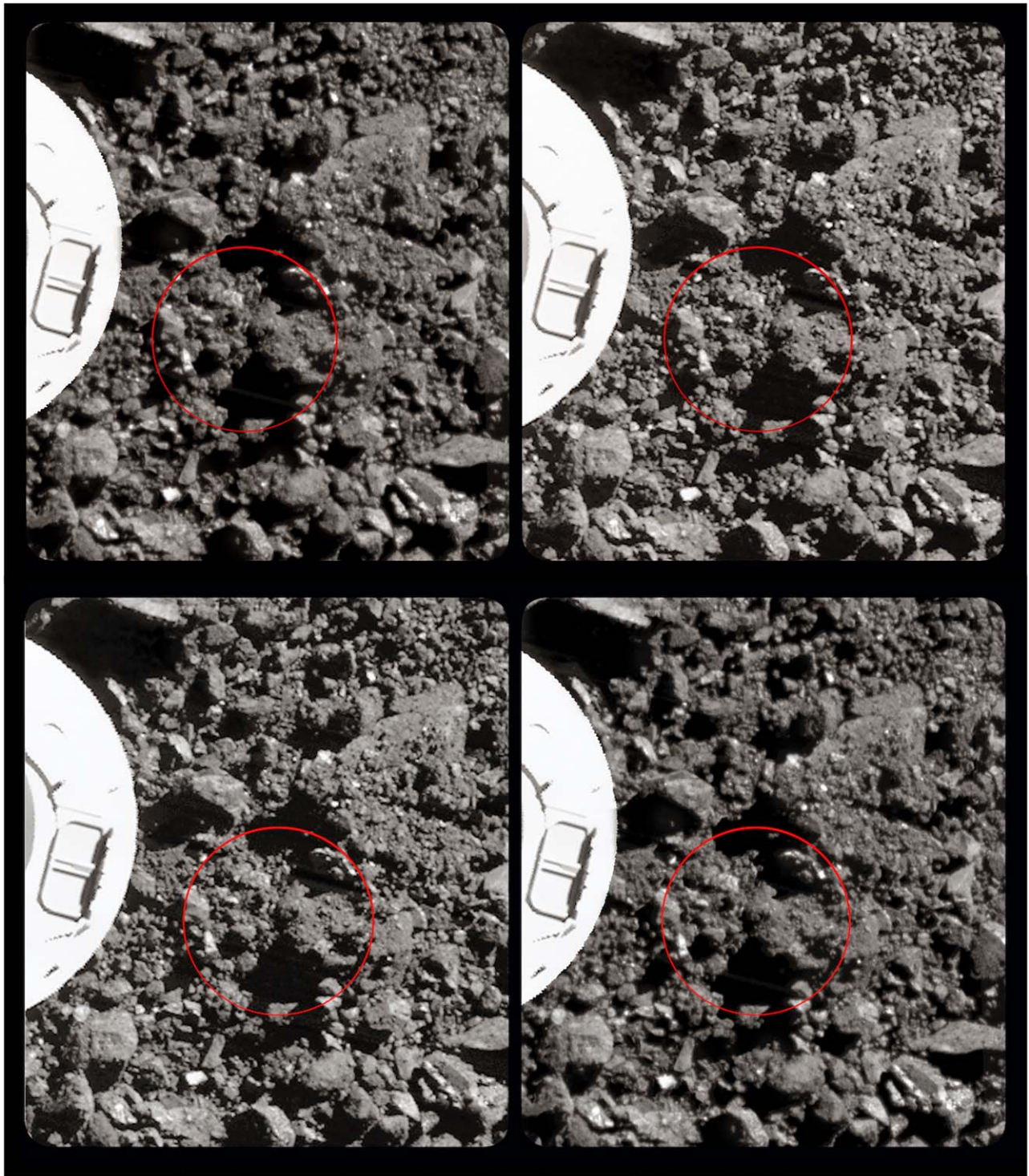


**Figure B4.** rms error for TAG spots exclusively inside (left) and outside (right) of the central 7 m of the crater (which includes the TAG observations). The black asterisk on both plots indicates the best-fit location when all spots are considered (Figure B3, Frame D). The red asterisk on the left figure indicates a second local minimum solution. However, fits to the full radiance spectrum using this minimum were much worse than when using the global minimum. The analysis of the spots outside of the sampleability region (right) revealed only one global minimum (red asterisk) which was within 3.5 cm of the global solution (black asterisk).

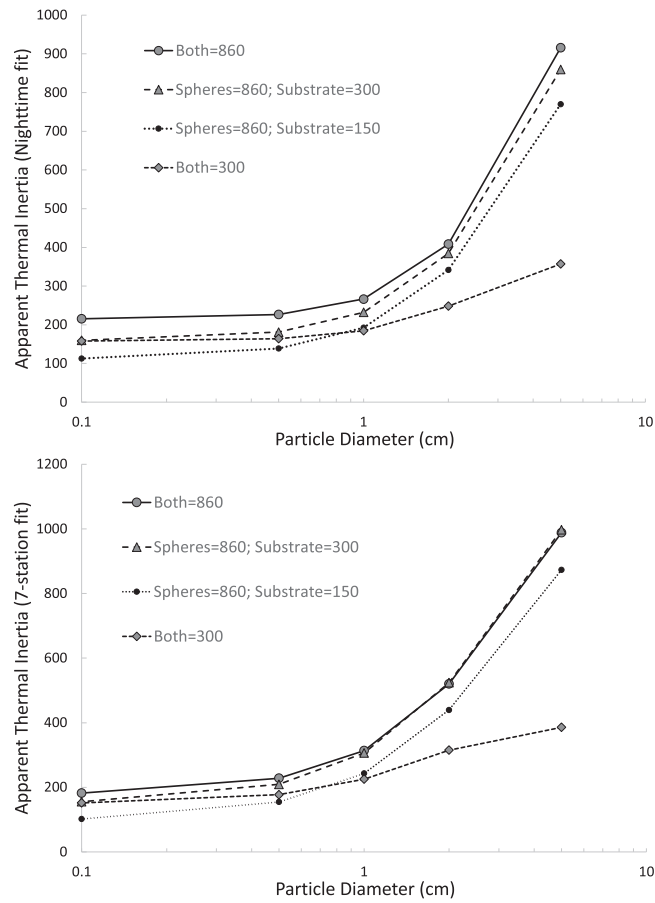


**Figure B5.** Thermal inertia results from this work (Matchpoint, Checkpoint, and TAG data) overlaid on thermal inertia values from Recon A and Recon B observations (Rozitis et al. 2022).

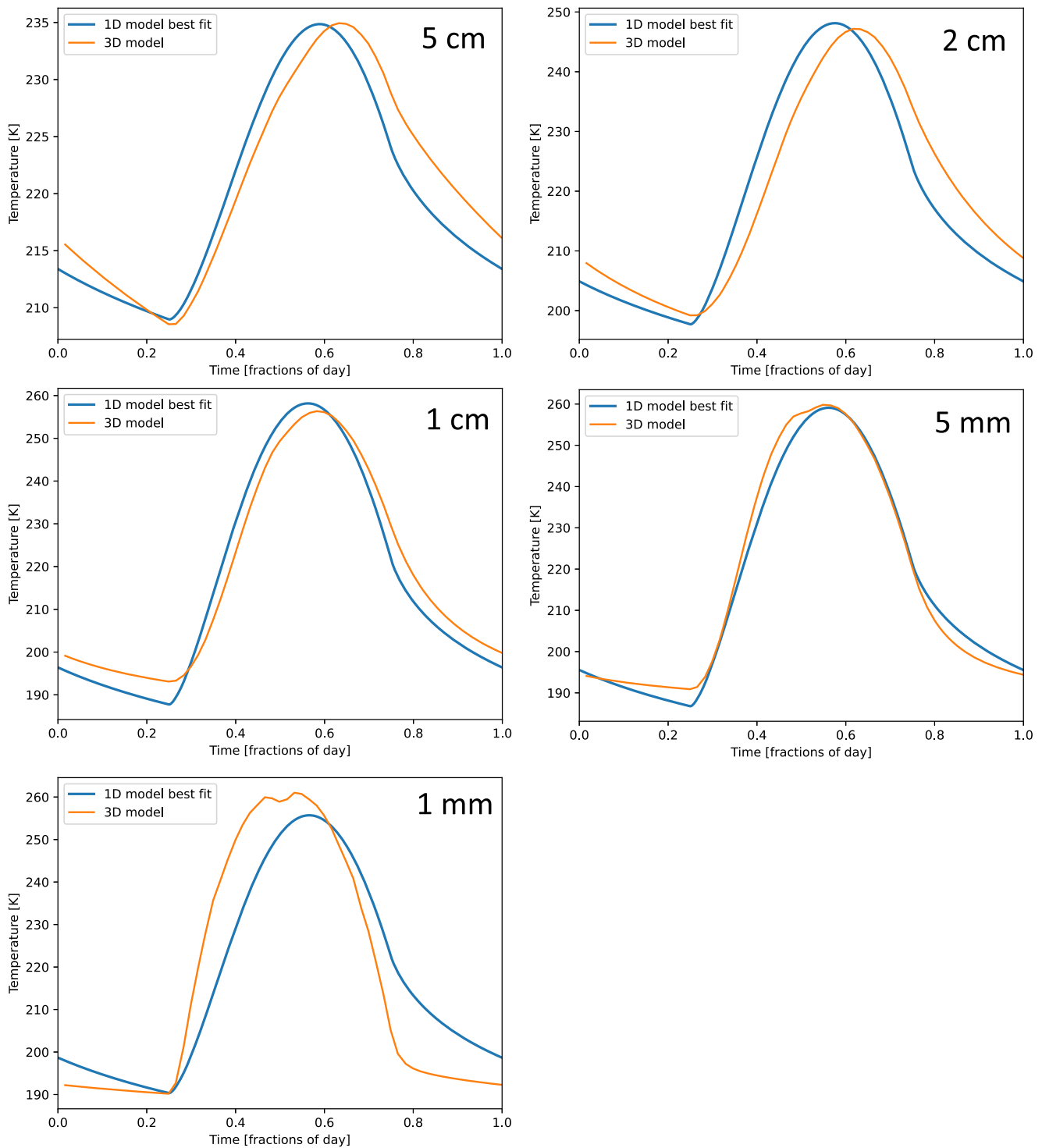




**Figure B6.** TAG site stereo-pair images. Top version can be viewed with a stereoscope, bottom version can be viewed cross-eyed. Figure adapted from Lauretta et al. (2023b).



**Figure B7.** Apparent thermal inertia of a rock covered with a dense monolayer of spherical particles. The unlayered thermal model was fit to the 3D model radiance at (top) local hour 3:20 AM and (bottom) to seven times of day corresponding to the OSIRIS-REx Detailed Survey stations. Particle sizes are 1 mm, 5 mm, 1 cm, 2 cm, and 5 cm. The thermal inertia of the individual particles, the rock substrate, or in some cases both sets of materials are indicated in the legend assuming standard units ( $\text{J m}^{-2} \text{K}^{-1} \text{s}^{-1/2}$ ). Compare to Figure 7 (daytime fit) in the main text.



**Figure B8.** 3D particle-coated model brightness temperature ( $10\ \mu\text{m}$ , orange) solutions where the thermal inertia of particles and the substrate is  $860\ \text{J m}^{-2}\ \text{K}^{-1}\ \text{s}^{-1/2}$ , as a function of particle size indicated in each plot. Best-fit thermal inertia solutions from the 1D model (fit to the local solar time of the TAG site observations, 14:40) are shown in blue. The small drop in temperature near noon for the cases with 1 mm and 5 mm sphere coatings is simply due to the ordered arrangement of the spheres. At that time, the direction of the Sun is aligned with the square pattern of the spheres such that they all briefly partially shadow each other, causing a temporary drop in temperature. This is not observed for the larger spheres because they have a larger volumetric heat capacity and thus do not respond as rapidly to shadowing.

#### ORCID iDs

Andrew J. Ryan <https://orcid.org/0000-0002-7535-8416>  
 Benjamin Rozitis <https://orcid.org/0000-0001-9893-241X>  
 Joshua P. Emery <https://orcid.org/0000-0001-9265-9475>  
 Marco Delbo <https://orcid.org/0000-0002-8963-2404>  
 Catherine M. Elder <https://orcid.org/0000-0002-9993-8861>

Dathon R. Golish <https://orcid.org/0000-0002-6159-539X>  
 Kevin J. Walsh <https://orcid.org/0000-0002-0906-1761>  
 Kenneth L. Edmundson <https://orcid.org/0000-0003-3666-0927>  
 Michael G. Daly <https://orcid.org/0000-0002-3733-2530>  
 Dante S. Laurretta <https://orcid.org/0000-0002-2597-5950>

## References

- Annex, A, Pearson, B, Seignovert, B, et al. 2020, *JOSS*, **5**, 2050
- Barnouin, O. S., Jawin, E. R., Daly, R. T., et al. 2022, *PSJ*, **3**, 75
- Becker, K. J., & Edmundson, K. L. 2024, arXiv:2401.12177
- Bennett, C. A., DellaGiustina, D. N., Becker, T. L., et al. 2021, *Icar*, **357**, 113690
- Biele, J., Burke, K. N., Grott, M., et al. 2020, AGUFM, P037–04
- Biele, J., Kührt, E., Senshu, H., et al. 2019, *PEPS*, **6**, 48
- Bierhaus, E. B., Clark, B. C., Harris, et al. 2018, *SSRv*, **214**, 107
- Burke, K. N., DellaGiustina, D. N., Bennett, C. A., et al. 2021, *RemS*, **13**, 1315
- Cambioni, S., Delbo, M., Poggiali, G., et al. 2021, *Natur*, **598**, 49
- Christensen, P. R., Hamilton, V. E., Anwar, S., Mehall, G., & Lauretta, D. S. 2019, OSIRIS-REx Thermal Emission Spectrometer (OTES) Bundle 11.0, NASA Planetary Data System, urn:nasa:pds:orex.otes:11.0
- Christensen, P. R., Hamilton, V. E., Mehall, G., et al. 2018, *SSRv*, **214**, 87
- Daly, M. G., Barnouin, O. S., Dickinson, C., et al. 2017, *SSRv*, **212**, 899
- Daly, M. G., Barnouin, O. S., Seabrook, J. A., et al. 2020, *SciA*, **6**, eabd3649
- DellaGiustina, D. N., Burke, K. N., Walsh, K. J., et al. 2020, *Sci*, **370**, eabc3660
- DellaGiustina, D. N., Emery, J. P., Golish, et al. 2019, *NatAs*, **3**, 341
- Digonnet, H., Silva, L., & Coupeuz, T. 2007, in AIP Conf. Proc. 908, Materials Processing and Design: Modeling, Simulation and Applications, ed. J. M. A. Cesar de Sa & A. D. Santos (Melville, NY: AIP), 269
- Edmundson, K. L., Becker, K. J., Becker, T. L., et al. 2020, *ISPA*, **V-3-2020**, 587
- Elder, C. 2024, LPSC, 55, 2590, <https://www.hou.usra.edu/meetings/lpsc2024/pdf/2590.pdf>
- Flynn, G. J., Consolmagno, G. J., Brown, P., & Macke, R. J. 2018, *ChEG*, **78**, 269
- Golish, D. R., Drouet d'Aubigny, C., Rizk, B., et al. 2020, *SSRv*, **216**, 12
- Grott, M., Knollenberg, J., Borgs, B., et al. 2017, *SSRv*, **208**, 413
- Grott, M., Knollenberg, J., Hamm, M., et al. 2019, *NatAs*, **3**, 971
- Hamilton, V. E., Christensen, P. R., Kaplan, H. H., et al. 2021, *A&A*, **650**, A120
- Hamilton, V. E., Simon, A. A., Christensen, P. R., et al. 2019, *NatAs*, **3**, 332
- Hamm, M., Grott, M., Senshu, H., et al. 2022, *NatCo*, **13**, 364
- Hamm, M., Hamilton, V. E., & Goodrich, C. A. 2023, *GeoRL*, **50**, e2023GL104795
- Hamm, M., Pelivan, I., Grott, M., & de Wiljes, J. 2020, *MNRAS*, **496**, 2776
- Ishizaki, T., Nagano, H., Tanaka, S., et al. 2023, *IJT*, **44**, 51
- Jawin, E., Ballouz, R.-L., Ryan, A. J., et al. 2023, *JGRE*, **128**, e2023JE008019
- Kieffer, H. H. 2013, *JGRE*, **118**, 451
- Lauretta, D. S., Adam, C. D., Allan, A. J., et al. 2022, *Sci*, **377**, 285
- Lauretta, D. S., Connolly, H. C., Jr, Grossman, J. N., et al. 2023a, arXiv:2308.11794
- Lauretta, D. S., May, B., Bennett, C. A., et al. 2023b, Benu 3-D: Anatomy of an Asteroid (Tucson, AZ: Univ. Arizona Press)
- Lauretta, D. S., DellaGiustina, D. N., Bennett, C. A., et al. 2019, *Natur*, **568**, 55
- Lauretta, D. S., Enos, H. L., Polit, A. T., et al. 2021, in Sample Return Missions: The Last Frontier of Solar System Exploration, ed. A. Longobardo (Amsterdam: Elsevier), 163
- Li, J.-Y., Zou, X.-D., Golish, D. R., et al. 2021, *PSJ*, **2**, 117
- Macke, R. J., Consolmagno, G. J., & Britt, D. T. 2011, *M&PS*, **46**, 1842
- Mitalas, G. P., & Stephenson, D. G. 1966, Fortran IV programs to calculate radiant energy interchange factors. DBR Computer Program, no. CP-25, National Research Council of Canada
- Nakamura, T., Matsumoto, M., Amano, K., et al. 2022, *Sci*, **379**, eabn8671
- Okada, T., Fukuhara, T., Taguchi, M., et al. 2017, *SSRv*, **208**, 255
- Opeil, C. P., Britt, D. T., Macke, R. J., & Consolmagno, G. J. 2020, *M&PS*, **55**
- Persson, B. N. J., & Biele, J. 2022, *AIPA*, **12**, 105307
- Rizk, B., d'Aubigny, C. D., Golish, D., et al. 2018, *SSRv*, **214**, 26
- Rozitis, B., Emery, J. P., Siegler, M. A., et al. 2020a, *JGRE*, **125**, e2019JE006323
- Rozitis, B., Ryan, A. J., Emery, J. P., et al. 2020b, *SciA*, **6**, eabc3699
- Rozitis, B., & Green, S. F. 2011, *MNRAS*, **415**, 2042
- Rozitis, B., Ryan, A. J., Emery, J. P., et al. 2022, *JGRE*, **127**, e2021JE007153
- Ryan, A. J., Pino Muñoz, D., Bernacki, M., & Delbo, M. 2020, *JGRE*, **125**, e2019JE006100
- Ryan, A. J., Pino Muñoz, D., Bernacki, M., et al. 2022, *JGRE*, **127**, e2022JE007191
- Ryan, A. J., Pino Muñoz, D., Rozitis, B., et al. 2024, Model Files: Rocks with Extremely Low Thermal Inertia at the OSIRIS-REx Sample Site on Asteroid Benu, v1.0, Figshare, [10.6084/m9.figshare.24535894](https://doi.org/10.6084/m9.figshare.24535894)
- Sakatani, N., Ogawa, K., Arakawa, M., & Tanaka, S. 2018, *Icar*, **309**, 13
- Sakatani, N., Tanaka, S., Okada, T., et al. 2021, *NatAs*, **5**, 766
- Scheeres, D. J., McMahon, J. W., French, A. S., et al. 2019, *NatAs*, **3**, 352
- Seabrook, J. A., Daly, M. G., Barnouin, O. S., et al. 2022, *PSJ*, **3**, 265
- Shimaki, Y., Senshu, H., Sakatani, N., et al. 2020, *Icar*, **348**, 113835
- Sugita, S., Honda, R., Morota, T., et al. 2019, *Sci*, **364**, eaaw0422
- Tricarico, P., Scheeres, D. J., French, A. S., et al. 2021, *Icar*, **370**, 114665
- Walsh, K. J., Ballouz, R. L., Jawin, E. R., et al. 2022, *SciA*, **8**, eabm6229
- Walsh, K. J., Jawin, E. R., Ballouz, R. L., et al. 2019, *NatGe*, **12**, 4